Article

Intrinsic Dynamic and Static Nature of π···π Interactions in Fused Benzene-Type Helicenes and Dimers, Elucidated with QTAIM Dual Functional Analysis

Taro Nishide and Satoko Hayashi *

Faculty of Systems Engineering, Wakayama University, 930 Sakaedani, Wakayama 640-8510, Japan;
s209004@wakayama-u.ac.jp
* Correspondence: hayashi3@sys.wakayama-u.ac.jp; Tel.: +81-73-457-8252

Abstract: The intrinsic dynamic and static nature of the π···π interactions between the phenyl groups in proximity of helicenes **3–12** are elucidated with the quantum theory of atoms-in-molecules dual functional analysis (QTAIM-DFA). The π···π interactions appear in C-∗-C, H-∗-H, and C-∗-H, with the asterisks indicating the existence of bond critical points (BCPs) on the interactions. The interactions of **3–12** are all predicted to have a p-CS/vdW nature (vdW nature of the pure closed-shell interaction), except for $^2C_{bay}$-∗-$^7C_{bay}$ of **10**, which has a p-CS/t-HB$_{nc}$ nature (typical-HBs with no covalency). (See the text for definition of the numbers of C and the bay and cape areas). The natures of the interactions are similarly elucidated between the components of helicene dimers **6:6** and **7:7** with QTAIM-DFA, which have a p-CS/vdW nature. The characteristic electronic structures of helicenes are clarified through the natures predicted with QTAIM-DFA. Some bond paths (BPs) in helicenes appeared or disappeared, depending on the calculation methods. The static nature of C_{cape}-∗-C_{cape} is very similar to that of C_{bay}-∗-C_{bay} in **9–12**, whereas the dynamic nature of C_{cape}-∗-C_{cape} appears to be very different from that of C_{bay}-∗-C_{bay}. The results will be a guide to design the helicene-containing materials of high functionality.

Keywords: ab initio calculations; quantum theory of atoms-in-molecules (QTAIM); nonbonded interactions; polycyclic aromatic hydrocarbon (PAH)

1. Introduction

Helicenes, which are ortho-fused polycyclic aromatic or heteroaromatic compounds with all rings angularly arranged to form helically shaped molecules, are of current and continuing interest. Helicenes are chiral; as a result, they are expected to have specific functionalities. Recently, helicenes have been widely applied in various fields [1–5], such as organic semiconductors [6–10], asymmetric catalysis [11–16], and molecular recognition [17–22], due to their diverse functionalities in materials. Many studies have also been reported on self-assembly phenomena at metal surfaces [23–26] caused by interactions with the π-orbitals of helicenes. The π-orbitals will cause intramolecular π···π interactions between adjacent aromatic rings of helicenes, which play an important role in effective interactions. It is crucial to clarify the nature of π···π interactions for future high-functioning material developments based on helicenes. The discussion in this paper will be limited to π···π interactions between the aromatic rings, the nature of which needs to be clarified, since helicenes of the fused benzene type were chosen as the target.

The noncovalent distances between the aromatic planes in close proximity to the helicenes were determined as the total effect of the attractive and repulsive forces between the atoms on the planes. The restoring forces from the deviated planarity in the helicenes should be a main factor for the attractive and repulsive forces due to π-orbital overlapping in the helicenes. The noncovalent distances between the planes in close proximity to the helicenes are defined as the balanced distances of the two factors. The noncovalent

intramolecular distances between atoms in close proximity to the helicenes must be (much) shorter than the noncovalent intermolecular distances between the unrestricted nonhelical aromatic species. The shorter distances in helicenes result from the $\pi\cdots\pi$ interactions between the planes in close proximity in space, which operate under very severe conditions. Clarifying the nature of the $\pi\cdots\pi$ interactions in helicenes under such severe conditions will enable us to understand the factors that control the structures and the nature of the interactions. The results will also provide a starting point for understanding the nature of $\pi\cdots\pi$ interactions and will hint at designs for materials with high functionality based on the interactions.

We have been particularly interested in the $\pi\cdots\pi$ interactions that operate under severe conditions, as these should be the factors that control the fine details of the structures. Interactions are also expected to result in materials with high functionalities. The nature of $\pi\cdots\pi$ interactions under such severe conditions was investigated in a series of fused benzene-type helicenes **1–12** and concave-type dimers **6:6–8:8** and **10:10**, where **1–3** are analyzed as helicenes in this paper, although they are usually not. Scheme 1 shows the structures of helicenes **1–12**, dimers **6:6–8:8**, **10:10**, and [*n*]phenacenes **1$_p$–12$_p$**, where **1$_p$–12$_p$** are the comparative compounds and **p** stands for phenacenes. The bay and cape areas used in this paper are also illustrated. We have previously reported the nature of the benzene $\pi\cdots\pi$ interactions in cyclophanes [27] (see also [28,29]). The $\pi\cdots\pi$ interactions in the helicenes must correspond to the extended $\pi\cdots\pi$ interactions of the species.
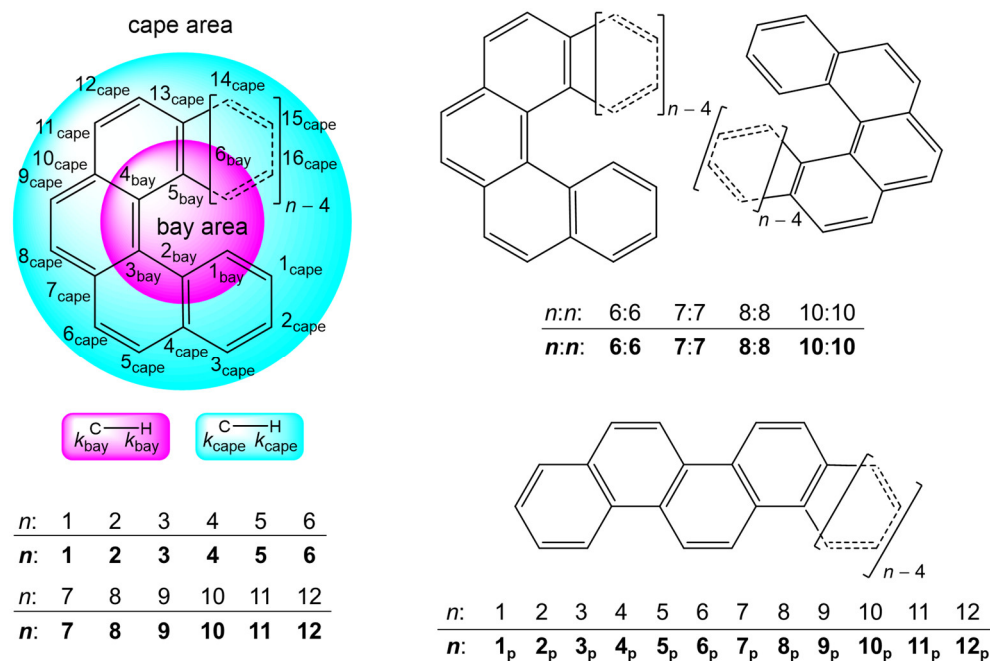
Scheme 1. Helicenes, **1–12**, dimers, **6:6–8:8** and **10:10**, and [*n*]phenacenes, **1$_p$–12$_p$**. The bay and cape areas in **1–12** are illustrated. The number of C is shown, where the number of H is the same for C–H. Benzene, naphthalene, and phenanthrene are defined corresponding to n = 1, 2, and 3, respectively.

The $\pi\cdots\pi$ interactions in the helicenes were analyzed with QTAIM dual functional analysis (QTAIM-DFA [30–35]), which we proposed based on the QTAIM approach introduced by Bader [36,37]. The $\pi\cdots\pi$ interactions will be reproduced on the bond paths (BPs) between atoms, where a bond critical point (BCP, ∗) appears on each BP. The $\pi\cdots\pi$ interactions in helicenes are typically described by BPs with BCPs of the H-∗-H, C-∗-H, and C-∗-C forms. The asterisk indicates the existence of a BCP in each BP [36,37]. In QTAIM-DFA, $H_b(r_c)$ is plotted versus $H_b(r_c)-V_b(r_c)/2$, where $H_b(r_c)$ and $V_b(r_c)$ are the total electron energy densities and potential energy densities, respectively, at the BCPs of

the interactions in question. In our treatment, data from the fully optimized structures and the perturbed structures surrounding the fully optimized structures are used for the plots.

Data from the fully optimized structures in the plots were analyzed using polar coordinate (R, θ) representation, which corresponds to the static nature of the interactions [30–35]. Data from both the perturbed and fully optimized structures are expressed by (θ_p, κ_p), where θ_p corresponds to the tangent line and κ_p is the curvature of the plot. θ and θ_p are measured from the y-axis and the y-direction, respectively. (See Figure SA1 of the Appendix S1 of the Supporting Information for the definition of the QTAIM-DFA parameters of (R, θ) and (θ_p, κ_p), along with Equations (SA3)–(SA6) and the footnotes of Table 1). The concept of the dynamic nature of the interactions was proposed based on (θ_p, κ_p). The θ_p and κ_p for the major bonds seem to be controlled by the characters of the local bonds in question: The influence from the behaviors of the minor bonds would not be so severe for usual cases.

Table 1. QTAIM Functions and QTAIM-DFA Parameters Evaluated for the Fused Benzene-Type Helicenes of Monomers (**3–12**), Employing the Perturbed Structures Generated with CIV [1–3].

Species	$\rho_b(r_c)$	$c\nabla^2\rho_b(r_c)$ [4]	$H_b(r_c)$	R [5]	θ [6]	C_{ii} [7]	θ_p [8]	κ_p [9]	Predicted Nature
X-∗-Y	(ea_o^{-3})	(au)	(au)	(au)	(°)	(Å mdyn^{-1})	(°)	(au^{-1})	
3 ($^1H_{bay}$-∗-$^4H_{bay}$)	0.0130	0.0060	0.0020	0.0063	71.3	3.29	72.8	12.4	p-CS/vdW
4 ($^1H_{bay}$-∗-$^5H_{bay}$)	0.0165	0.0078	0.0026	0.0082	71.8	6.67	74.5	11.4	p-CS/vdW
5 ($^1H_{bay}$-∗-$^6C_{bay}$)	0.0131	0.0063	0.0021	0.0066	71.6	6.12	80.8	136	p-CS/vdW
6 ($^1H_{bay}$-∗-$^5C_{bay}$)	0.0131	0.0060	0.0020	0.0063	71.3	3.82	79.9	31.8	p-CS/vdW
7 ($^1H_{bay}$-∗-$^6C_{bay}$)	0.0135	0.0063	0.0021	0.0067	71.5	5.47	77.9	188	p-CS/vdW
7 ($^2C_{bay}$-∗-$^7C_{bay}$)	0.0114	0.0051	0.0017	0.0054	71.9	3.33	80.6	128	p-CS/vdW
8 ($^1H_{bay}$-∗-$^6C_{bay}$)	0.0130	0.0061	0.0021	0.0065	71.1	5.51	76.7	189	p-CS/vdW
8 ($^2C_{bay}$-∗-$^7C_{bay}$)	0.0117	0.0052	0.0017	0.0055	71.8	2.01	86.4	28.5	p-CS/vdW
9 ($^1H_{bay}$-∗-$^5C_{bay}$)	0.0134	0.0062	0.0022	0.0066	70.7	3.40	79.5	627	p-CS/vdW
9 ($^2C_{bay}$-∗-$^7C_{bay}$)	0.0113	0.0050	0.0016	0.0053	72.1	1.83	81.6	119	p-CS/vdW
9 ($^3C_{bay}$-∗-$^8C_{bay}$)	0.0122	0.0053	0.0016	0.0056	72.9	1.87	85.0	196	p-CS/vdW
9 ($^4C_{cape}$-∗-$^{22}C_{cape}$) [10]	0.0055	0.0020	0.0007	0.0022	70.7	5.25	66.9	135	p-CS/vdW
9 ($^6C_{cape}$-∗-$^{23}C_{cape}$)	0.0061	0.0021	0.0007	0.0022	70.4	8.51	69.4	37.7	p-CS/vdW
10 ($^1H_{bay}$-∗-$^6C_{bay}$)	0.0137	0.0064	0.0021	0.0067	71.6	5.74	79.2	123	p-CS/vdW
10 ($^2C_{bay}$-∗-$^7C_{bay}$) [11]	0.0113	0.0050	0.0018	0.0053	70.5	1.86	94.2	2890	p-CS/t-HB$_{nc}$
10 ($^3C_{bay}$-∗-$^8C_{bay}$)	0.0114	0.0050	0.0016	0.0053	72.1	1.78	82.0	182	p-CS/vdW
10 ($^6C_{cape}$-∗-$^{23}C_{cape}$)	0.0059	0.0020	0.0007	0.0021	70.4	9.02	69.7	7.0	p-CS/vdW
10 ($^7C_{cape}$-∗-$^{25}C_{cape}$)	0.0061	0.0022	0.0008	0.0024	70.3	3.42	68.0	10.3	p-CS/vdW
11 ($^1H_{bay}$-∗-$^6C_{bay}$)	0.0136	0.0063	0.0021	0.0067	71.6	5.41	79.8	113	p-CS/vdW
11 ($^2C_{bay}$-∗-$^7C_{bay}$)	0.0116	0.0051	0.0017	0.0054	71.5	1.84	87.1	142	p-CS/vdW
11 ($^3C_{bay}$-∗-$^8C_{bay}$)	0.0115	0.0050	0.0016	0.0053	72.0	1.91	82.6	166	p-CS/vdW
11 ($^4C_{bay}$-∗-$^9C_{bay}$)	0.0111	0.0049	0.0016	0.0052	71.7	1.69	79.5	155	p-CS/vdW
11 ($^4C_{cape}$-∗-$^{22}C_{cape}$)	0.0053	0.0019	0.0007	0.0020	70.1	6.81	68.3	13.5	p-CS/vdW
11 ($^6C_{cape}$-∗-$^{23}C_{cape}$)	0.0059	0.0020	0.0007	0.0021	70.2	10.21	69.7	7.5	p-CS/vdW
11 ($^7C_{cape}$-∗-$^{25}C_{cape}$)	0.0059	0.0022	0.0008	0.0023	70.2	3.58	67.8	7.2	p-CS/vdW
11 ($^9C_{cape}$-∗-$^{26}C_{cape}$)	0.0062	0.0021	0.0007	0.0022	70.4	5.80	69.5	64.7	p-CS/vdW
12 ($^1H_{bay}$-∗-$^6C_{bay}$)	0.0136	0.0063	0.0021	0.0067	71.5	4.84	80.5	103	p-CS/vdW
12 ($^2C_{bay}$-∗-$^7C_{bay}$)	0.0115	0.0051	0.0017	0.0053	71.5	1.77	87.8	349	p-CS/vdW
12 ($^3C_{bay}$-∗-$^8C_{bay}$)	0.0117	0.0051	0.0016	0.0053	72.3	1.74	83.6	241	p-CS/vdW
12 ($^4C_{bay}$-∗-$^9C_{bay}$)	0.0110	0.0048	0.0016	0.0051	71.5	1.72	80.7	87.8	p-CS/vdW
12 ($^4C_{cape}$-∗-$^{22}C_{cape}$)	0.0055	0.0020	0.0007	0.0022	70.2	4.80	66.3	697	p-CS/vdW
12 ($^6C_{cape}$-∗-$^{23}C_{cape}$)	0.0060	0.0021	0.0008	0.0022	70.0	6.78	68.0	8.6	p-CS/vdW
12 ($^7C_{cape}$-∗-$^{25}C_{cape}$)	0.0059	0.0022	0.0008	0.0023	70.0	3.41	68.2	3.3	p-CS/vdW
12 ($^9C_{cape}$-∗-$^{26}C_{cape}$)	0.0059	0.0020	0.0007	0.0021	70.3	6.95	69.4	24.7	p-CS/vdW
12 ($^{10}C_{cape}$-∗-$^{28}C_{cape}$)	0.0056	0.0020	0.0007	0.0022	70.5	4.09	68.6	65.4	p-CS/vdW

[1] Calculated with M06-2X/6-311+G(3d,p). [2] Data are given at the BCPs. [3] All interactions are predicted to have the p-CS/vdW nature, except for **10** ($^2C_{bay}$-∗-$^7C_{bay}$), which has the p-CS/t-HB$_{nc}$ nature. [4] $c\nabla^2\rho_b(r_c) = H_b(r_c) - V_b(r_c)/2$, where $c = \hbar^2/8m$. [5] $R = (x^2 + y^2)^{1/2}$, where $(x, y) = (H_b(r_c) - V_b(r_c)/2, H_b(r_c))$. [6] $\theta = 90° - \tan^{-1}(y/x)$. [7] $C_{ij} = \partial^2 E/\partial f_i \partial f_j$, where i and j refer to internal coordinates, and the external force components acting on the system f_i and f_j correspond to i and j, respectively. [8] $\theta_p = 90° - \tan^{-1}(dy/dx)$. [9] $\kappa_p = ?d^2y/dx^2?/[1 + (dy/dx)^2]^{3/2}$. [10] Data from $w = \pm 0.0125, \pm 0.025$, and 0 were used for the plot since BCPs were not detected at $w = \pm 0.05$. [11] Data from $w = -0.05, -0.0375, -0.025, -0.0125$, and 0 were used for the plot since BCPs were not detected when $w > 0$.

The perturbed structures necessary for QTAIM-DFA were generated by CIV [38], with the coordinates $\mathbf{C}_i$ corresponding to the compliance constants C_{ii} for the internal vibrations [39–44]. The basic concept for the compliance constants was introduced by Taylor and Pitzer [45], followed by Konkoli and Cremer [46]. The C_{ij} are defined as the partial second derivatives of the potential energy due to an external force [47–49], where i and j refer to internal coordinates. The dynamic nature of the interactions based on perturbed structures with CIV is described as the "intrinsic dynamic nature of interactions" because the coordinates are invariant to the choice of coordinate system. QTAIM-DFA and the criteria obtained by applying QTAIM-DFA with CIV to standard interactions are explained in the Appendix of the Supporting Information using Schemes SA1–SA3, Figure SA1 and SA2, Table SA1, and Equations (SA1)–(SA7).

In this work, we present the results of the investigations into the natures of the $\pi\cdots\pi$ interactions in **1–12**, **6:6–8:8**, and **10:10**, although some are discussed in the Supporting Information or calculated only for comparison. The interactions are classified and characterized by using the criteria as a reference. The structural features and the energy profile are also discussed to provide a solid basis for the discussion.

2. Methodological Details of the Calculations

Calculations were performed with the Gaussian 09 program package [50]. The 6-311+G(3d,p) basis set was used for the calculations at the DFT level of M06-2X [51] (M06-2X/6-311+G(3d,p)). The optimized structures were confirmed by frequency analysis. The results of the frequency analysis were used to calculate the compliance constants (C_{ii}) and the coordinates corresponding to C_{ii} ($\mathbf{C}_i$). Calculations were also performed with M06-2X/6-311+G(2d,p) and LC-ωPBE/6-311+G(2d,p) [52] to examine the basis set and level dependence, containing the optimized $\pi\cdots\pi$ distances, on the results. The results with M06-2X/6-311+G(3d,p) are discussed in the text, while the results with M06-2X/6-311+G(2d,p) and LC-ωPBE/6-311+G(2d,p) are discussed mainly in the Supporting Information. We should be careful with the basis set and level dependence on the QTAIM-DFA parameters, which has been examined carefully [53]. Similar methodology was also employed for the theoretical studies of the π-stacking [54,55].

Equation (1) explains the method for generating perturbed structures with CIV [38]. The i-th perturbed structure in question ($\mathbf{S}_{iw}$) is generated by adding $\mathbf{C}_i$ to the standard orientation of a fully optimized structure ($\mathbf{S}_o$) in the matrix representation. The coefficient g_{iw} in Equation (1) controls the structural difference between $\mathbf{S}_{iw}$ and $\mathbf{S}_o$, g_{iw} is determined to satisfy Equation (2) for r, where r and r_o stand for the interaction distances in question in the perturbed and fully optimized structures, respectively, with $a_o = 0.52918$ Å (Bohr radius). Five-digit $\mathbf{C}_i$ values were used to predict $\mathbf{S}_{iw}$.

$$\mathbf{S}_{iw} = \mathbf{S}_o + g_{iw}\cdot\mathbf{C}_i \tag{1}$$

$$r = r_o + wa_o \ (w = (0), \pm0.025 \text{ and } \pm0.05; a_o = 0.52918 \text{ Å}) \tag{2}$$

$$y = c_o + c_1x + c_2x^2 + c_3x^3 \ (R_c^2\text{: square of the correlation coefficient}) \tag{3}$$

The QTAIM functions were calculated using the same basis set system as in the optimizations, unless otherwise noted, and were analyzed with the AIM2000 [56,57] and AIMAll [58] programs. The $H_b(\mathbf{r}_c)$ values are plotted versus the $H_b(\mathbf{r}_c) - V_b(\mathbf{r}_c)/2$ values for five data points in Equation (2) in QTAIM-DFA: $w = 0, \pm0.025$, and ±0.05. Each plot was analyzed using a cubic function regression curve, as shown in Equation (3), where $(x, y) = (H_b(\mathbf{r}_c) - V_b(\mathbf{r}_c)/2, H_b(\mathbf{r}_c))$ ($R_c^2 > 0.99999$ as usual) [31].

3. Results and Discussion

3.1. Structural Features of **1–12** and Their Energy Profile

The structures of **1–12** were optimized with M06-2X/6-311+G(3d,p), M06-2X/6-311+G(2d,p), and LC-ωPBE/6-311+G(2d,p), retaining C_2 symmetry. The selected noncovalent X⋯Y distances (X, Y = C, H) in the optimized structures with M06-2X/6-311+G(3d,p), M06-

2X/6-311+G(2d,p), and LC-ωPBE/6-311+G(2d,p) are shown in Table S1 of the Supporting Information, along with the observed values [59–66].

How can the behaviour of the energies of the helicenes be explained? The energies of the helicenes were compared with the energies of [n]phenacene, a nonhelical species, evaluated with M06-2X/6-311+G(3d,p). The energy profiles will be discussed based on the energy differences, $\Delta E(n) = E(n) - E(n - 1)$ for helicenes (**1–12**) and $\Delta E(n_p) = E(n_p) - E(n_p - 1)$ for [n]phenacenes (**1_p–12_p**). The $\Delta E(n)$ values correspond to the energy differences in the formation of **n** from **$n − 1$**, and the $\Delta E(n_p)$ values similarly correspond to n_p from ($n_p - 1$). The $E(n)$, $E(n_p)$, $\Delta E(n)$, and $\Delta E(n_p)$ values were calculated on the energy surface, which are described by $E_{ES}(n)$, $E_{ES}(n_p)$, $\Delta E_{ES}(n)$, and $\Delta E_{ES}(n_p)$, respectively. The values were also calculated with the zero-point energies, which are described by $E_{ZP}(n)$, $E_{ZP}(n_p)$, $\Delta E_{ZP}(n)$, and $\Delta E_{ZP}(n_p)$. The values calculated with M06-2X/6-311+G(3d,p) are collected in Table S2 of the Supporting Information. The plot of $\Delta E_{ZP}(n)$ versus $\Delta E_{ES}(n)$ revealed an excellent correlation ($y = 1.0042x + 0.6859$; $R_c^2 = 0.980$, see Figure S1 of the Supporting Information). As a result, $\Delta E_{ES}(n)$ can be used to analyze the energy terms.

Figure 1 shows the plots of $\Delta E_{ES}(n)$ and $\Delta E_{ES}(n_p)$ versus n. Both the $\Delta E_{ES}(n)$ and $\Delta E_{ES}(n_p)$ values ($\Delta E_{ES}(n; n_p)$) decrease when n increases from 2 to 3. The extension of the π system appears to contribute more to the formation of phenanthrene from naphthalene than the repulsive noncovalent H···H interaction. The $\Delta E_{ES}(\mathbf{3}; \mathbf{3_p})$ values are less than the $\Delta E_{ES}(\mathbf{2}; \mathbf{2_p})$ values; however, the $\Delta E_{ES}(n; n_p)$ values increase from $\mathbf{3}; \mathbf{3_p}$ to $\mathbf{4}; \mathbf{4_p}$. In the case of $\Delta E_{ES}(n_p)$, the $\Delta E_{ES}(\mathbf{4_p})$ value is somewhat larger than $\Delta E_{ES}(\mathbf{3_p})$ but slightly smaller than $\Delta E_{ES}(\mathbf{2_p})$. The $\Delta E_{ES}(n_p)$ value decreases again slightly from $\mathbf{4_p}$ to $\mathbf{5_p}$. Then, the values are nearly constant for $n_p \geq \mathbf{5_p}$. The results show that the repulsive energy from the noncovalent H···H interaction does not appear to be as severe as the stabilization factor from the extended π systems in **1_p–12_p**. Namely, the n_p system stabilizes almost constantly as the size of the species increase, especially for $n_p \geq \mathbf{5_p}$, although a change in $\Delta E_{ES}(n_p)$ is detected for $\mathbf{2_p} \leq n_p < \mathbf{5_p}$.
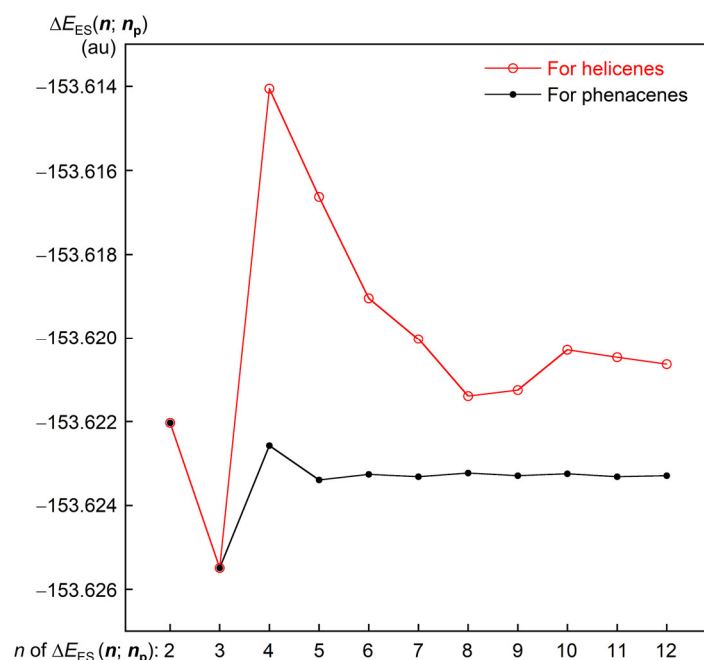

Figure 1. Plot of $\Delta E_{ES}(n)$ and $\Delta E_{ES}(n_p)$ versus n, evaluated with M06-2X/6-311+G(3d,p), where $\Delta E_{ES}(n) = E_{ES}(n) - E_{ES}(n - 1)$ and $\Delta E_{ES}(n_p) = E_{ES}(n_p) - E_{ES}(n_p - 1)$.

The data points for $\Delta E_{ES}(n)$ appear to be greater than those for $\Delta E_{ES}(n_p)$ when $n \geq 4$. The observations must be due to the severe steric repulsion in $\Delta E_{ES}(n \geq \mathbf{4})$, where the plot for $\Delta E_{ES}(n_p)$ corresponds to that without such severe steric repulsion. The $\Delta E_{ES}(\mathbf{4})$ value is

much larger than those of $\Delta E_{ES}(\mathbf{2})$ and $\Delta E_{ES}(\mathbf{3})$. The results can be explained by considering the much larger contribution from the repulsive noncovalent H$\cdots$H interaction in **4** than in **3**. This consideration is supported by the optimized structure of **4**, drawn in Figure 2, as the molecular graph type. The $\Delta E_{ES}(\pmb{n})$ values decrease in the following order: $\Delta E_{ES}(\mathbf{4}) >$ $\Delta E_{ES}(\mathbf{5}) > \Delta E_{ES}(\mathbf{6}) > \Delta E_{ES}(\mathbf{7}) > \Delta E_{ES}(\mathbf{8})$. The contribution of steric repulsion to $\Delta E_{ES}(\pmb{n})$ due to noncovalent interactions is expected to increase as *n* increases in this process. However, the observed results are the opposite of what was expected. Therefore, the observed trend should be attributed to the increased energy-lowering effect by the extended π systems in **4–8** relative to the repulsive interactions.
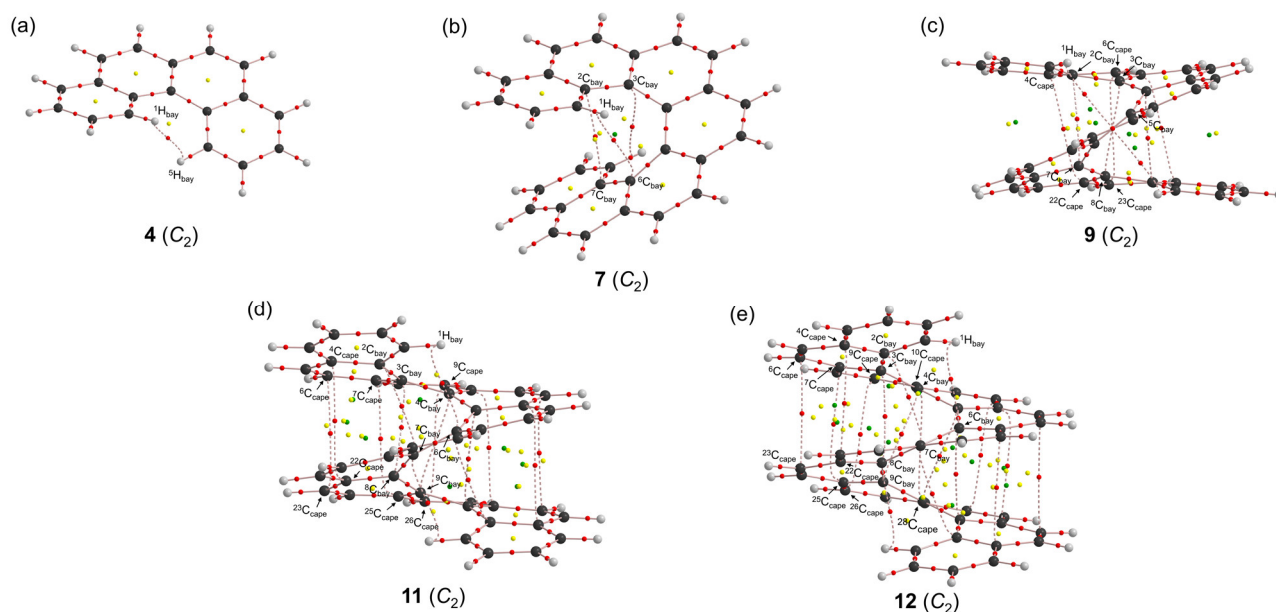

Figure 2. Molecular graphs for **4** (**a**), **7** (**b**), **9** (**c**), **11** (**d**), and **12** (**e**), calculated with M06-2X/6-311+G(3d,p), where BPs with BCPs corresponding to intramolecular noncovalent interactions are detected. The BCPs are denoted by red dots, RCPs (ring critical points) by yellow dots, CCPs (cage critical points) by green dots, and BPs by pink lines. The carbon atoms are in black and the hydrogen atoms are in grey.

The $\Delta E_{ES}(\pmb{n})$ value becomes somewhat larger again from *n* = **8** to **9** and **9** to **10**, and then decreases again from **10** to **11** and **11** to **12**. The subtle conditions in the steric repulsion contribute to the complex behaviour of $\Delta E_{ES}(\pmb{n})$ ($8 \le n \le 12$). The behaviour of $\Delta E_{ES}(\mathbf{2})$–$\Delta E_{ES}(\mathbf{12})$ shown in Figure 1 should be affected both by the repulsive factor of the noncovalent H-∗-H, C-∗-H, and C-∗-C interactions and by the energy-lowering factor of the extended π system. The $\Delta E_{ES}(\mathbf{4})$ value is the largest among $\Delta E_{ES}(\mathbf{2})$–$\Delta E_{ES}(\mathbf{12})$. The results are of great interest since the repulsive noncovalent H$\cdots$H interaction in **4** from **3** appears to be very large among **2–12** when evaluated by $\Delta E_{ES}(\pmb{n})$. The trend in $\Delta E_{ES}(\pmb{n})$ seems to be in good agreement with those reported by Rulíšek et al., calculated with PBE-D/TZVP//PBE-D/6-31G(d), except for $\Delta E_{ES}(\mathbf{8})$ and $\Delta E_{ES}(\mathbf{9})$ [67].

It is also instructive to analyze the aromaticities of acenes, phenacenes, and helicenes after investigating the energy profiles. The structures of acenes, phenacenes, and helicenes are illustrated in Chart S1 of the Supporting Information, together with the definition of the ring positions. The aromaticities were analyzed by the HOMA (harmonic oscillator model of aromaticity) method [68]. The HOMA values are collected in Table S3 of the Supporting Information. The HOMA values of the acenes and phenacenes are plotted versus those of the helicenes, which are shown in Figure S2 of the Supporting Information. The plot of the data for phenacenes versus those for helicenes gave a very good correlation ($y = 0.964x +$ 0.042; $R_c^2 = 0.981$), whereas the correlations of the plots for acenes versus helicenes were very poor ($y = -0.685x + 0.995$; $R_c^2 = 0.492$ if calculated under the closed–shell singlet

conditions and $y = -0.399x + 0.880$; $R_c^2 = 0.317$ under the open–shell singlet conditions). The very good correlation of the former demonstrates that the aromaticities of the helicenes appear to be very similar to those of the phenacenes, irrespective of the very severe steric deformations in the structures of helicenes. However, the very poor correlations with the negative correlation constants show that the aromaticities of the helicenes are very different from those of acenes.

3.2. Survey of X-∗-Y (X, Y = C and H) in 3–12 with the Molecular Graphs

Figure 2 shows the molecular graphs, exemplified by **4**, **7**, **9**, **11**, and **12**. Many BPs with BCPs are detected in the π⋯π interactions between the phenyl rings in close proximity to the helicenes. The molecular graphs for helicenes **3–12**, except for **4**, **7**, **9**, **11**, and **12**, are shown in Figure S3 of the Supporting Information.

The BPs corresponding to X-∗-Y (X, Y = C and H) appear almost straight, as shown in Figure 2 and Figure S4 of the Supporting Information, although some appear somewhat bent. To examine the linearity of the BPs further, the lengths of the BPs (r_{BP}) were calculated for all X-∗-Y of **3–12**, along with the corresponding straight-line distances (R_{SL}). The values are collected in Table S4 of the Supporting Information, along with the differences between them ($\Delta r_{BP} = r_{BP} - R_{SL}$). The averaged values of Δr_{BP} were 0.2040, 0.4006, 0.0588, and 0.1451 Å for H_{bay}-∗-H_{bay}, C_{bay}-∗-H_{bay}, C_{bay}-∗-C_{bay}, and C_{cape}-∗-C_{cape}, respectively. As a result, Δr_{BP} for H_{bay}-∗-H_{bay} and C_{bay}-∗-H_{bay} were larger than 0.20 Å, while those for C_{bay}-∗-C_{bay} and C_{cape}-∗-C_{cape} were less than 0.15 Å. Therefore, the BPs corresponding to C_{bay}-∗-C_{bay} and C_{cape}-∗-C_{cape} can be roughly approximated as straight lines since the Δr_{BP} values are less than 0.20 Å (see also Figure S4 of the Supporting Information).

The QTAIM functions were calculated at BCPs on X-∗-Y of **3–12** with M06-2X/6-311+G(3d,p). Table 1 collects the $\rho_b(r_c)$, $H_b(r_c) - V_b(r_c)/2$, and $H_b(r_c)$ values for one of the X-∗-Y if it is doubly degenerated due to the C_2 symmetry of the optimized structures. Figure 3 shows the plots of $H_b(r_c)$ versus $H_b(r_c) - V_b(r_c)/2$ for each X-∗-Y, exemplified by **3–6**, **8**, **10**, and **12**, where H-∗-H was detected in **3** and **4** and C-∗-H and C-∗-C were detected in **8**, **10**, and **12**. (See Figure S5 of the Supporting Information for **7**, **9**, and **11**).
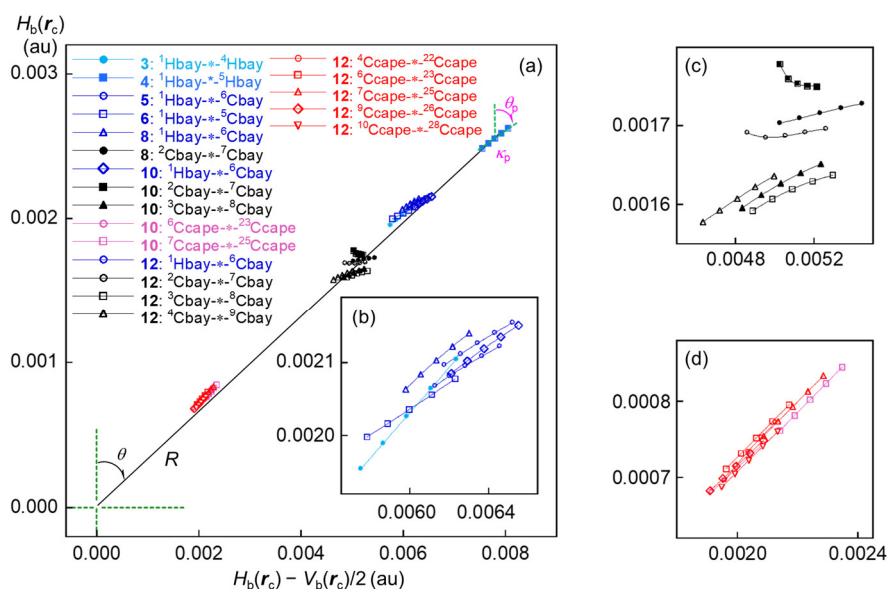
Figure 3. Plots of $H_b(r_c)$ versus $H_b(r_c) - V_b(r_c)/2$ for H-∗-H, C-∗-H, and C-∗-C, exemplified by those in **3–6**, **8**, **10**, and **12**. (**a**) Whole picture; (**b**) Magnified picture of the C-∗-H area; (**c**) Magnified picture of the C-∗-C bay area; (**d**) Magnified picture of the C-∗-C cape area. The definitions of (R, θ) and (θ_p, κ_p) are illustrated, exemplified by H-∗-H in **4**.

The plots were analyzed according to Equations (SA3)–(SA6) of the Supporting Information. Table 1 also collects the QTAIM-DFA parameters of (R, θ) and (θ_p, κ_p) for each X-*-Y of **3**–**12**, along with the C_{ii} values corresponding to the interactions in question. The (θ_p, κ_p) values, evaluated with CIV, should be denoted by $(\theta_{p:CIV}, \kappa_{p:CIV})$, respectively. However, (θ_p, κ_p) will be used in place of $(\theta_{p:CIV}, \kappa_{p:CIV})$ to simplify the notation. The QTAIM functions and QTAIM-DFA parameters calculated with M06-2X/6-311+G(2d,p) and LC-ωPBE/6-311+G(2d,p) are collected in Tables S5 and S6 of the Supporting Information respectively.

3.3. Nature of Each X-*-Y in **3**–**12**

The criteria shown in Scheme SA3 and Table SA1 of the Supporting Information indicate that the interactions in the range of $45° < \theta < 90°$ should be classified as pure closed-shell (*p*-CS) interactions. In the *p*-CS region of $45° < \theta < 90°$, the character of the interactions will be the vdW type for $45° < \theta_p < 90°$ ($45° < \theta < 75°$), whereas the character of the interactions will be the typical hydrogen bond type (*t*-HB) with no covalency (*t*-HB$_{nc}$) for $90° < \theta_p < 125°$ ($75° < \theta < 90°$), where $\theta = 75°$ and $\theta_p = 125°$ are tentatively given for $\theta_p = 90°$ and $\theta = 90°$, respectively.

The C atoms in helicenes **3**–**12** were subdivided into C_{bay} and C_{cape} based on the positions of the atoms in the species, as were the H atoms into H_{bay} and H_{cape}. The bay and cape areas (positions) in the species are illustrated in Scheme 1. While both the C_{bay} and C_{cape} atoms of **3**–**12** participate in the interactions as BPs, only H_{bay} atoms participate as BPs. The θ and θ_p values for H-*-H, C-*-H, and C-*-C of **3**–**12**, collected in Table 2, are all less than 90°, except for θ_p of $^2C_{bay}$-*-$^7C_{bay}$ in **10**, where $(\theta, \theta_p) = (70.5°, 94.2°)$. The $^2C_{bay}$-*-$^7C_{bay}$ interaction in **10** is denoted by **10** ($^2C_{bay}$-*-$^7C_{bay}$) (see also Table 1). Therefore, the H-*-H, C-*-H, and C-*-C interactions of **3**–**12** are all classified as *p*-CS interactions and characterized to have a vdW nature, which is denoted by *p*-CS/vdW, except for **10** ($^2C_{bay}$-*-$^7C_{bay}$), which is predicted to have a *p*-CS/*t*-HB$_{nc}$ nature.

Table 2. QTAIM Functions and QTAIM-DFA Parameters Evaluated for the Fused Benzene-Type Helicenes of Concave-Type Dimers (**6:6** and **7:7**), Employing the Perturbed Structures Generated with CIV [1–3].

Species	$\rho_b(r_c)$	$c\nabla^2\rho_b(r_c)$	$H_b(r_c)$	R	θ	C_{ii}	θ_p	κ_p	Predicted Nature
X-*-Y	(ea_o^{-3})	(au)	(au)	(au)	(°)	(Å mdyn^{-1})	(°)	(au^{-1})	
6:6 ($^1H_{bay}$-*-$^{17'}H_{cape}$) [4]	0.0045	0.0018	0.0006	0.0019	72.6	25.02	88.1	5163	*p*-CS/vdW
6:6 ($^1H_{cape}$-*-$^{17'}H_{cape}$)	0.0061	0.0022	0.0006	0.0023	74.3	35.63	76.2	184.2	*p*-CS/vdW
6:6 ($^1H_{cape}$-*-$^{16'}H_{cape}$)	0.0051	0.0019	0.0007	0.0020	70.9	42.01	74.9	69.9	*p*-CS/vdW
6:6 ($^{15}C_{cape}$-*-$^{17'}C_{cape}$) [5]	0.0065	0.0025	0.0009	0.0027	69.2	12.64	70.8	1066	*p*-CS/vdW
6:6 ($^{16}C_{cape}$-*-$^{17'}C_{cape}$)	0.0066	0.0026	0.0010	0.0028	68.3	8.63	68.0	53.5	*p*-CS/vdW
6:6 ($^1H_{bay}$-*-$^5C_{bay}$)	0.0128	0.0057	0.0019	0.0060	71.9	3.817	78.3	32.3	*p*-CS/vdW
6:6 ($^3C_{bay}$-*-$^7H_{bay}$)	0.0134	0.0061	0.0020	0.0064	71.7	3.414	79.3	29.5	*p*-CS/vdW
7:7 ($^{20}H_{cape}$-*-$^{18'}H_{cape}$)	0.0073	0.0031	0.0012	0.0033	68.9	14.61	75.5	24.6	*p*-CS/vdW
7:7 ($^{20}H_{cape}$-*-$^{20'}H_{cape}$)	0.0054	0.0022	0.0008	0.0024	70.0	27.90	72.7	36.5	*p*-CS/vdW
7:7 ($^{20}H_{cape}$-*-$^{2'}C_{cape}$)	0.0079	0.0030	0.0010	0.0032	71.4	10.01	73.3	125.7	*p*-CS/vdW
7:7 ($^{18}H_{cape}$-*-$^{3'}C_{cape}$)	0.0050	0.0016	0.0005	0.0016	73.8	17.36	73.2	181.8	*p*-CS/vdW
7:7 ($^1H_{bay}$-*-$^6C_{bay}$)	0.0132	0.0062	0.0021	0.0065	70.8	5.557	80.0	93.5	*p*-CS/vdW
7:7 ($^3C_{bay}$-*-$^8H_{bay}$)	0.0138	0.0065	0.0021	0.0068	71.9	5.024	78.8	154.1	*p*-CS/vdW

[1] Calculated with M06-2X/6-311+G(3d,p). [2] Data are given at the BCPs. [3] See footnotes of Table 1 for the QTAIM-DFA parameters and C_{ii}. [4] Data from $w = -0.0375, -0.025, -0.0125, 0$, and 0.0125 were used for the plot, since BCPs for **6:6** ($^1H_{bay}$-*-$^{17'}H_{cape}$) were not detected when $w > 0.0125$. [5] Data from $w = -0.05, -0.0375, -0.025, -0.0125$, and 0 were used for the plot, since BCPs for **6:6** ($^{15}C_{cape}$-*-$^{17'}C_{cape}$) were not detected when $w > 0$.

Next, the interactions were individually examined. The (θ, θ_p) values are $(71.3°, 72.8°)$ and $(71.8°, 74.5°)$ for **3** ($^1H_{bay}$-*-$^4H_{bay}$) and **4** ($^1H_{bay}$-*-$^5H_{bay}$), respectively. The θ values for **3** ($^1H_{bay}$-*-$^4H_{bay}$) and **4** ($^1H_{bay}$-*-$^5H_{bay}$) are larger than those of A-*-HF (A = He, Ne, and Ar: $(\theta, \theta_p) = (59.9–70.9°, 64.0–88.0°)$), whereas the θ_p values are larger than those of

A-∗-HF (A = He and Ar). The interaction in **4** is estimated to be slightly stronger than that in **3**, although the real image of **3** (^{1}H$_{bay}$-∗-^{4}H$_{bay}$) has been much debated [69–71]. The detection of BPs with BCPs for **3** (^{1}H$_{bay}$-∗-^{4}H$_{bay}$) would not show enough strength for the interaction. It could be the mathematical results of the treatment. Nevertheless, **3** (^{1}H$_{bay}$-∗-^{4}H$_{bay}$) and **4** (^{1}H$_{bay}$-∗-^{5}H$_{bay}$) are discussed as very weak interactions in this work because the (θ, θ_p) values are larger than those of A-∗-HF (A = He, Ne, and Ar). Double H$_{bay}$-∗-C$_{bay}$ interactions are detected for each of **5–12**, with (θ, θ_p) values of (70.7–71.6°, 76.7–80.8°). The (θ, θ_p) values are very close to those of A-∗-HF (A = He, Ne, and Ar). The BP (H$_{bay}$-∗-C$_{bay}$) in **6** and **9** connect the H$_{bay}$ and C$_{bay}$ atoms. However, they are not located at the nearest positions, as shown in Table 1 and Figure S3 of the Supporting Information. Therefore, the BP (H$_{bay}$-∗-C$_{bay}$) in **6** and **9** should be analyzed carefully.

One, one, four, four, seven, and eight different types of C-∗-C interactions are detected for **7–12**, respectively. The (θ, θ_p) values for C-∗-C in **7–12** are (70.0–72.9°, 66.3–94.2°). It appears better to separately examine the values for two groups of C$_{bay}$-∗-C$_{bay}$ and C$_{cape}$-∗-C$_{cape}$. While the (θ, θ_p) values of C$_{bay}$-∗-C$_{bay}$ in **7–12** are (71.5–72.9°, 79.5–87.8°), the values are (70.0–70.7°, 66.3–69.7°) for C$_{cape}$-∗-C$_{cape}$. The θ values for C$_{cape}$-∗-C$_{cape}$ are slightly smaller than those of C$_{bay}$-∗-C$_{bay}$ (by 0.5–2.2°), but the θ_p values for C$_{cape}$-∗-C$_{cape}$ are much smaller than those of C$_{bay}$-∗-C$_{bay}$ (by 13.2–24.5°). In this case, $\theta_p < \theta$ for C$_{cape}$-∗-C$_{cape}$, whereas $\theta_p > \theta$ for C$_{bay}$-∗-C$_{bay}$. Interactions with $\theta_p > \theta$ are usually observed, but interactions with $\theta_p < \theta$ are rare.

Interactions with $\theta > \theta_p$ occur under some specific conditions. To examine the behaviour of θ and θ_p in **7–12**, the $\Delta\theta_p$ (=$\theta_p - \theta$) values are plotted versus θ_p for C-∗-C, H-∗-H and C-∗-H in **3–12**. Figure 4 shows this plot. The plot showed a very good correlation for all data ($y = 0.918x - 64.88$: $R_c^2 = 0.995$). (A substantial correlation was not found in the plot of $\Delta\theta_p$ versus θ due to the very small range of θ). The two areas for C-∗-C interactions with $\Delta\theta_p > 0$ and $\Delta\theta_p < 0$ are clearly illustrated by the green dotted lines in Figure 4. The $\Delta\theta_p$ values for the interactions are positive if the θ_p values are larger than 70.7°, whereas $\Delta\theta_p < 0$ if $\theta_p < 70.7°$. Figure 4 clearly shows that C$_{bay}$-∗-C$_{bay}$ and C$_{cape}$-∗-C$_{cape}$ in **9–12** belong to the areas where $\Delta\theta_p > 0$ and $\Delta\theta_p < 0$, respectively.
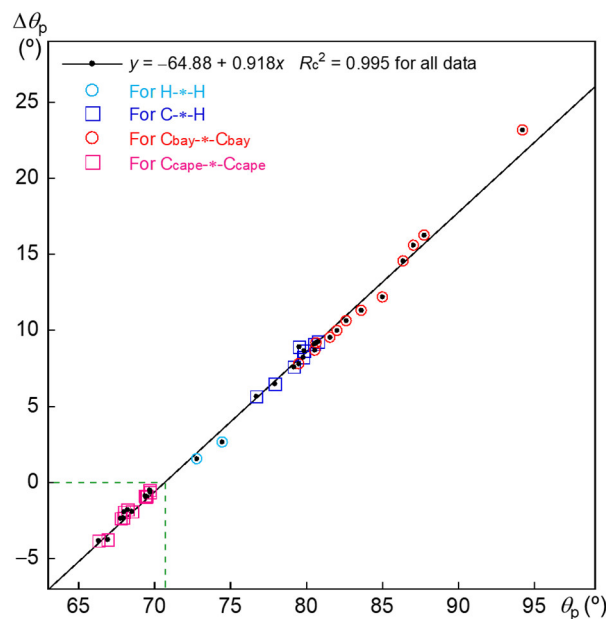
Figure 4. Plot of $\Delta\theta_p$ versus θ_p for H-∗-H, C-∗-H, and C-∗-C in **3–12**, evaluated with M06-2X/6-311+G(3d,p), where $\Delta\theta_p = (\theta_p - \theta)$.

It seems difficult to clearly explain the results shown in Figure 4; however, our explanation is as follows: The static nature of the interactions described by θ should be a measure of the strength of the interactions. If so, the steric compression on C$_{cape}$-∗-C$_{cape}$

in **9**–**12** appears to be similar to that on C_{bay}-∗-C_{bay} in fully optimized structures. Namely, the C_{cape}-∗-C_{cape} and C_{bay}-∗-C_{bay} interactions in the fully optimized structures of **9**–**12** would be affected similarly to steric compression, according to the θ values. On the other hand, the dynamic nature of the interactions is defined by θ_p based on the behaviour of the interactions in the perturbed structures. The C_{bay}-∗-C_{bay} interactions in the perturbed structures will be affected by steric compression, similar to the usual cases of interactions, whereas the C_{cape}-∗-C_{cape} interactions will be inversely affected compared with the usual cases when measured by the θ_p values at the BCPs of the interactions.

*3.4. Nature of Each X-∗-Y in **6**:**6** and **7**:**7***

What is the behaviour of the interactions when the helicenes form concave-type dimers? The behaviour was elucidated, exemplified by **6**:**6** (C_i) and **7**:**7** (C_i) with M06-2X/6-311+G(3d,p). Figure 5 shows molecular graphs of **6**:**6** and **7**:**7**. Five and four independent BPs with BCPs were detected in **6**:**6** and **7**:**7**, respectively, between the components of H-∗-H and C-∗-H, as well as two independent BPs with BCPs for the intramolecular C-∗-H interactions in each component of **6**:**6** and **7**:**7**. The behaviour of the interactions was also investigated for **7**:**7** (C_i), **8**:**8** (C_i), and/or **10**:**10** (C_i) with M06-2X/6-311+G(2d,p) and LC-ωPBE/6-311+G(2d,p). The results are collected in Tables S7 and S8 of the Supporting Information. The QTAIM functions were similarly calculated for the intermolecular interactions at the BCPs on the BPs of **6**:**6** and **7**:**7** with M06-2X/6-311+G(3d,p).
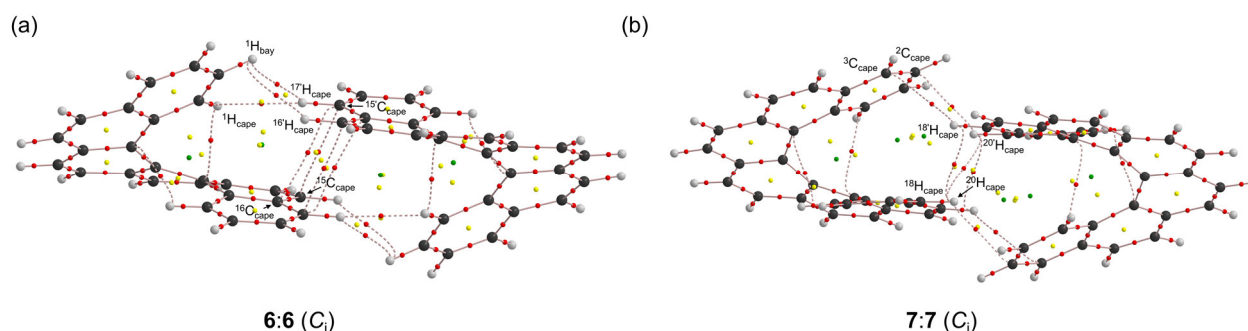
(a)   (b)

6:**6** (C_i)   **7**:**7** (C_i)

Figure 5. Molecular graphs for helicene dimers, **6**:**6** (**a**) and **7**:**7** (**b**), calculated with M06-2X/6-311+G(3d,p), where BPs with BCPs corresponding to intra- and intermolecular noncovalent interactions are detected. The BCPs are denoted by red dots, RCPs (ring critical points) by yellow dots, CCPs (cage critical points) by green dots, and BPs by pink lines. The carbon atoms are in black and the hydrogen atoms are in grey.

Table 2 collects the $\rho_b(r_c)$, $H_b(r_c) - V_b(r_c)/2$, and $H_b(r_c)$ values for one of the doubly degenerate interactions due to the C_i symmetry of the optimized structures. Figure 6 shows the plots of $H_b(r_c)$ versus $H_b(r_c) - V_b(r_c)/2$ for each interaction between the components at **6**:**6** and **7**:**7**. (The plots for **8**:**8** and **10**:**10** are shown in Figure S7 of the Supporting Information, and the data are collected in Table S8 of the Supporting Information).

The plots were analyzed similarly to the case of **3**–**12**. Table 2 also collects the QTAIM-DFA parameters of (R, θ) and (θ_p, κ_p) for the intermolecular interactions in question at **6**:**6** and **7**:**7**, together with the C_{ii} values corresponding to the interactions in question. The (θ, θ_p) values for the three H-∗-H and two C-∗-C intermolecular independent interactions of **6**:**6** are (70.9–74.3°, 74.9–88.1°) and (68.3–69.2°, 68.0–70.8°), respectively. The (θ, θ_p) values for the couple of H-∗-H and two C-∗-H intermolecular independent interactions at **7**:**7** are (68.9–70.0°, 72.7–75.5°) and (71.4–73.8°, 73.2–73.3°), respectively. The θ and θ_p values for the intermolecular H-∗-H, C-∗-H, and C-∗-C interactions at **6**:**6** and **7**:**7** are all less than 90°; therefore, the interactions are all predicted to have a *p*-CS/vdW nature (see Table 2). The interactions appear to be very weak, based on the (θ, θ_p) values. However, $(\theta, \theta_p) = (72.6°, 88.1°)$ for **6**:**6** ($^1H_{bay}$-∗-$^{17'}H_{cape}$), of which nature seems close to *p*-CS/*t*-HB$_{nc}$.
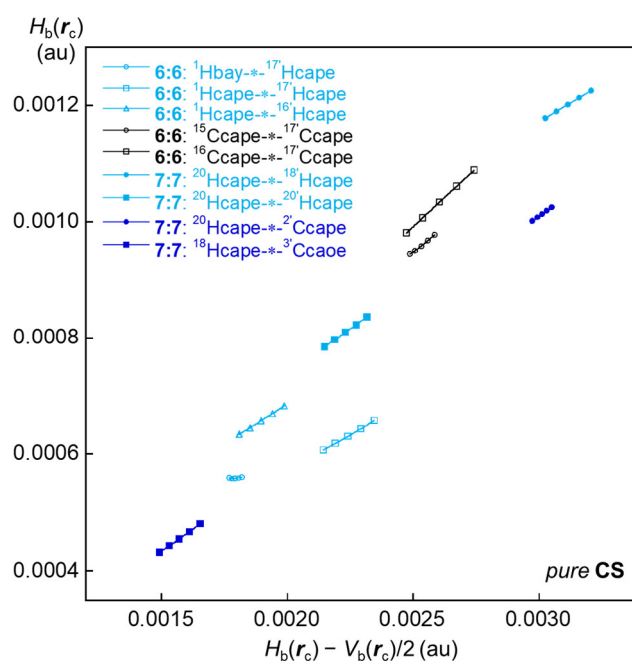
Figure 6. Plots of $H_b(r_c)$ versus $H_b(r_c) - V_b(r_c)/2$ for H-∗-H, C-∗-H, and C-∗-C at **6:6** (C_i) and **7:7** (C_i), calculated with M06-2X/6-311+G(3d,p).

In the case of intramolecular interactions, $^1H_{bay}$-∗-$^5C_{bay}$ and $^3C_{bay}$-∗-$^7H_{bay}$ were detected at **6:6**. The former was also observed in **6**, whereas the latter was newly detected in **6:6**. The new appearance of **6** ($^3C_{bay}$-∗-$^7H_{bay}$) may be due to a structural change at **6:6** relative to **6**. Similarly, $^1H_{bay}$-∗-$^6C_{bay}$ and $^3C_{bay}$-∗-$^8H_{bay}$ were detected at **7:7**. The former was observed in **7**, while $^3C_{bay}$-∗-$^8H_{bay}$ in **7:7** appeared in place of $^2C_{bay}$-∗-$^7C_{bay}$ in **7**. The change in the optimized structures between **7** and **7:7** would again be responsible for the results. However, clarifying the reason for the appearance/disappearance of BPs is very complex and difficult in helicenes, and it is beyond the scope of this work.

Highly theoretical treatment must be necessary to clarify the reason for the appearance and disappearance of BPs/BCPs. Pendás and coworkers discussed BPs as privileged exchange channels, using the interacting quantum atom (IQA) framework [72]. They have investigated how BPs between an atom A and atoms B in its environment appear to be determined by competition among the A–B exchange correlation energies that always contribute to stabilize the A–B interactions. And they have predicted that a BP is found between two atoms by examining a number of archetypal simple systems: (1) there is no other competing atom in its vicinity, so there must be a direct exchange route between them or (2) its V_{xc} term is the largest among several possibilities, where V_{xc} stands for a quantum-mechanical correction coming from the exchange correlation second-order density [72]. It has also indicated that interaction energies between both atoms cannot be universally used to predict the existence of a BP between them [73]. Moreover, they are not correlated to distances or to the density values at BCPs. On the contrary, the exchange contribution is shown to be an appropriate descriptor [73]. Similarly, theoretical treatments are applied to various interactions, employing QTAIM-defined an atomic interaction line (AIL: Presence or absence), IQA-defined interaction energy and its components, NCI (non-covalent interactions)-defined isosurfaces, and deformation density [74]. The reason for the appearance and disappearance of BPs/BCPs in the helicenes would be rationalized by applying above theory [27].

The (θ, θ_p) values for the intramolecular interactions at **6:6** and **7:7** are (70.8–71.9°, 78.3–80.0°). As a result, the interactions are all predicted to have a *p*-CS/vdW nature (see Table 2). The predicted natures of the interactions in **6:6** and **7:7** appear to be similar to those in **6** and **7**, perhaps due to the very weak nature of both dimers and monomers.
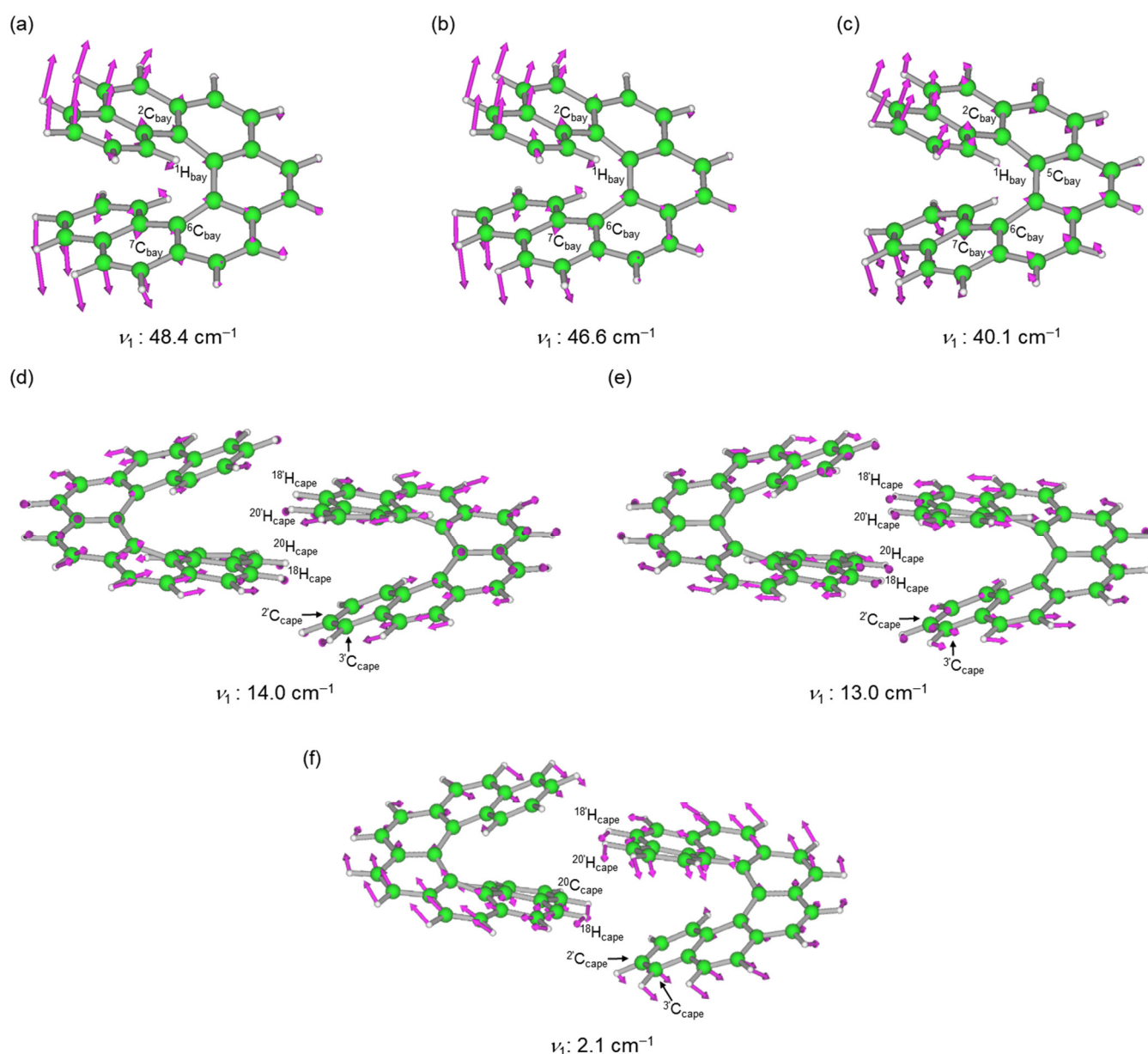
4. Basis Set and Level Dependence of the Predicted Natures

The basis set and level dependence of the predicted natures was investigated, exemplified by **7** and **7:7**, to attempt to determine the reason why the optimized structures can easily change. Table 3 shows the QTAIM-DFA parameters of (R, θ) and (θ_p, κ_p) and the C_{ii} values, calculated with M06-2X/6-311+G(3d,p), M06-2X/6-311+G(2d,p), and LC-ωPBE/6-311+G(2d,p). Table 3 includes the distances in question as well as some internal vibration(s) ν_n corresponding to the interactions in question, which are closely related to (θ_p, κ_p). Figure 7 shows the motions of the internal vibrations for ν_1 of **7** and **7:7** calculated with M06-2X/6-311+G(3d,p), M06-2X/6-311+G(2d,p), and LC-ωPBE/6-311+G(3d,p). (Other motions are shown in Figure S9 of the Supporting Information).

Table 3. QTAIM Functions and QTAIM-DFA Parameters Evaluated for the Fused Benzene-Type Helicene (**7**) and the Concave-Type Dimer (**7:7**), Employing the Perturbed Structures Generated with CIV, together with the X-∗-Y Distances and the Corresponding Internal Vibrations, with the Frequencies Closely Related to the Interactions in Question [1,2].

Species	$r(\text{X}\cdots\text{Y})$	R	θ	C_{ii}	θ_p	κ_p	Predicted Nature
X-∗-Y	(Å)	(au)	(°)	(Å mdyn^{-1})	(°)	(au^{-1})	
		7 (M06-2X/6-311+G(3d,p): $\nu_1 = 43.4$ cm^{-1})					
^{1}H$_{\text{bay}}$-∗-^{6}C$_{\text{bay}}$	2.5902	0.0067	71.5	5.47	77.9	187.5	p-CS/vdW
^{2}C$_{\text{bay}}$-∗-^{7}C$_{\text{bay}}$	2.9751	0.0054	71.9	3.33	80.6	128.2	p-CS/vdW
		7 (M06-2X/6-311+G(2d,p): $\nu_1 = 46.6$ cm^{-1})					
^{1}H$_{\text{bay}}$-∗-^{6}C$_{\text{bay}}$	2.5896	0.0067	70.4	5.49	81.6	39.9	p-CS/vdW
^{2}C$_{\text{bay}}$-∗-^{7}C$_{\text{bay}}$	3.0025	0.0054	69.9	3.06	78.7	120.2	p-CS/vdW
		7 (LC-ωPBE/6-311+G(2d,p): $\nu_1 = 40.1$ cm^{-1}) [3,4]					
^{1}H$_{\text{bay}}$-∗-^{5}C$_{\text{bay}}$	2.4681	0.0066	70.5	3.72	82.2	46.4	p-CS/vdW
		7:7 (M06-2X/6-311+G(3d,p): $\nu_1 = 14.0$ cm^{-1}; $\nu_4 = 24.2$ cm^{-1}; $\nu_5 = 29.3$ cm^{-1}; $\nu_{11} = 81.2$ cm^{-1})					
^{20}H$_{\text{cape}}$-∗-$^{18'}$H$_{\text{cape}}$	2.5423	0.0033	68.9	14.61	75.5	24.6	p-CS/vdW
^{20}H$_{\text{cape}}$-∗-$^{20'}$H$_{\text{cape}}$	2.7155	0.0024	70.0	27.90	72.7	36.5	p-CS/vdW
^{20}H$_{\text{cape}}$-∗-$^{2'}$C$_{\text{cape}}$	2.6769	0.0032	71.4	10.01	73.3	125.7	p-CS/vdW
^{18}H$_{\text{cape}}$-∗-$^{3'}$C$_{\text{cape}}$	2.9640	0.0016	73.8	17.36	73.2	181.8	p-CS/vdW
		7:7 (M06-2X/6-311+G(2d,p): $\nu_1 = 13.0$ cm^{-1}; $\nu_4 = 22.1$ cm^{-1}; $\nu_5 = 27.3$ cm^{-1}; $\nu_{11} = 78.6$ cm^{-1})					
^{20}H$_{\text{cape}}$-∗-$^{18'}$H$_{\text{cape}}$	2.5643	0.0032	67.9	16.63	75.2	60.1	p-CS/vdW
^{20}H$_{\text{cape}}$-∗-$^{20'}$H$_{\text{cape}}$	2.7287	0.0024	68.6	29.20	71.9	42.2	p-CS/vdW
^{20}H$_{\text{cape}}$-∗-$^{2'}$C$_{\text{cape}}$	2.6881	0.0031	70.2	11.44	69.4	12.4	p-CS/vdW
^{18}H$_{\text{cape}}$-∗-$^{3'}$C$_{\text{cape}}$	2.9857	0.0016	73.0	31.43	73.2	181.9	p-CS/vdW
		7:7 (LC-ωPBE/6-311+G(2d,p): $\nu_1 = 2.1$ cm^{-1}; $\nu_5 = 15.8$ cm^{-1}; $\nu_6 = 28.8$ cm^{-1}; $\nu_8 = 48.2$ cm^{-1}) [5,6]					
^{20}C$_{\text{cape}}$-∗-$^{18'}$H$_{\text{cape}}$	3.2357	0.0015	63.8	65.63	67.4	40.4	p-CS/vdW
^{20}H$_{\text{cape}}$-∗-$^{20'}$H$_{\text{cape}}$	3.0148	0.0014	63.6	96.42	66.9	90.7	p-CS/vdW
^{20}H$_{\text{cape}}$-∗-$^{2'}$C$_{\text{cape}}$	3.0656	0.0014	67.2	52.66	70.0	10.9	p-CS/vdW
^{18}H$_{\text{cape}}$-∗-$^{3'}$C$_{\text{cape}}$	3.6594	0.0005	62.9	73.99	73.9	394.0	p-CS/vdW

[1] See footnotes of Table 1 for the QTAIM-DFA parameters and C_{ii}. [2] The motions of the internal vibrations are shown in Figure 7 and Figure S9 of the Supporting Information. [3] BPs and BCPs were not detected for ^{1}H$_{\text{bay}}$-∗-^{6}C$_{\text{bay}}$ and ^{2}C$_{\text{bay}}$-∗-^{7}C$_{\text{bay}}$. [4] $r(^1$H$_{\text{bay}}$-∗-^{6}C$_{\text{bay}}) = 2.5609$ Å and $r(^2$C$_{\text{bay}}$-∗-^{7}C$_{\text{bay}}) = 3.2265$ Å. [5] BPs and BCPs were not detected for ^{20}H$_{\text{cape}}$-∗-$^{18'}$H$_{\text{cape}}$. [6] $r(^{20}$H$_{\text{cape}}$-∗-$^{18'}$H$_{\text{cape}}) = 2.9473$ Å.

Figure 7. The internal vibrational motions of ν_1 for **7** (C_2) and **7:7** (C_i). (**a**) For **7** (C_2) calculated with M06-2X/6-311+G(3d,p); (**b**) for **7** (C_2) calculated with M06-2X/6-311+G(2d,p); (**c**) for **7** (C_2) calculated with LC-ωPBE/6-311+G(2d,p); (**d**) for **7:7** (C_i) calculated with M06-2X/6-311+G(3d,p); (**e**) for **7:7** (C_i) calculated with M06-2X/6-311+G(2d,p); (**f**) for **7:7** (C_i) calculated with LC-ωPBE/6-311+G(2d,p).

The calculated $r(^1H_{bay}\cdots^6C_{bay})$ and $r(^2C_{bay}\cdots^7C_{bay})$ distances were 2.590 Å and 2.975 Å, respectively, for **7**, when calculated with M06-2X/6-311+(3d,p), while the values were 2.590 Å and 3.003 Å, respectively, when calculated with M06-2X/6-311+(2d,p). The differences are less than 0.001 Å for $r(^1H_{bay}\cdots^6C_{bay})$ and 0.028 Å for $r(^2C_{bay}\cdots^7C_{bay})$. The results show that the structure of **7** optimized with M06-2X/6-311+(2d,p) appears to be nearly identical to that optimized with M06-2X/6-311+(3d,p). On the other hand, the $r(^1H_{bay}\cdots^6C_{bay})$ and $r(^2C_{bay}\cdots^7C_{bay})$ of **7** were 2.561 Å and 3.227 Å, respectively, if calculated with LC-ωPBE/6-311+(2d,p). The difference was −0.029 Å for the former but 0.224 Å for the latter relative to the corresponding values calculated with M06-2X/6-311+(2d,p). The structure of **7** optimized with LC-ωPBE/6-311+(2d,p) appears to be (very) different from that optimized with M06-2X/6-311+(2d,p), especially around $r(^2C_{bay}\cdots^7C_{bay})$. In the case of $^1H_{bay}\cdots^5C_{bay}$, the distance was optimized to be 2.468 Å with LC-ωPBE/6-311+(2d,p),

which is shorter than the $r(^1H_{bay}\cdots^6C_{bay})$ distance optimized with M06-2X/6-311+(2d,p) (2.590 Å) by 0.122 Å. BPs (with BCPs) were detected for $^1H_{bay}$-∗-$^6C_{bay}$ and $^2C_{bay}$-∗-$^7C_{bay}$ in **7** if calculated with M06-2X/6-311+(3d,p) and M06-2X/6-311+(2d,p), while a BP was detected for $^1H_{bay}$-∗-$^5C_{bay}$ if calculated with LC-ωPBE/6-311+(2d,p). The $^2C_{bay}$-∗-$^7C_{bay}$ and $^1H_{bay}$-∗-$^5C_{bay}$ distances in **7**, optimized with LC-ωPBE/6-311+(2d,p), were (much) longer and shorter than those optimized with M06-2X/6-311+(2d,p), respectively.

The differences in the optimized distances appear to be the main factor for the appearance/disappearance of the BPs, although predicting the appearance/disappearance of the BPs is very difficult and complex. Despite such different results, the motion of ν_1 appears to be very similar when calculated at both the M06-2X and LC-ωPBE levels, indicating that ν_1 is a good measure for imaging the dynamic nature of the $\pi\cdots\pi$ interactions in **7** among the internal vibrations. Small differences in the dynamic nature of the interactions predicted at both the M06-2X and LC-ωPBE levels result from the (very) similar motion of ν_1. The magnitudes of the displacements in the cape area seem (much) larger than those in the bay area in ν_1. This will be instructive if the relationship is clarified for that between the magnitudes of the displacements and the $\Delta\theta_p$ values. This issue will be investigated in a future work. The very low energy of ν_1 in **7** suggests the basis set and level dependence can easily change the optimized structure.

In the case of **7:7**, the $r(^{20}H_{cape}\cdots^{18}H_{cape})$, $r(^{20}H_{cape}\cdots^{20'}H_{bay})$, $r(^{20}H_{cape}\cdots^{2'}C_{cape})$, and $r(^8H_{cape}\cdots^{3'}C_{cape})$ distances were 2.543 Å, 2.716 Å, 2.677 Å, and 2.964 Å, respectively, when calculated with M06-2X/6-311+(3d,p), while the values were 2.564 Å, 2.729 Å, 2.688 Å, and 2.986 Å, respectively, when calculated with M06-2X/6-311+(2d,p). The differences are 0.011–0.022 Å, which are less than approximately 0.02 Å. The results show that the optimized structures of **7:7** are very similar with both M06-2X/6-311+(3d,p) and M06-2X/6-311+(2d,p). On the other hand, the distances are optimized to be 2.947 Å, 3.015 Å, 3.066 Å, and 3.659 Å with LC-ωPBE/6-311+(2d,p). The differences with the corresponding values of M06-2X/6-311+(2d,p) are 0.286–0.674 Å. Namely, the structure of **7:7** optimized with LC-ωPBE/6-311+(2d,p) appears to be very different from that optimized with M06-2X/6-311+(2d,p), similar to the case of **7**.

The $^{20}C_{cape}$-∗-$^{18'}H_{cape}$ distance was optimized to be 3.236 Å, which is longer than $r(^{20}H_{cape}\cdots^{18'}H_{cape})$ (2.947 Å) by 0.288 Å with LC-ωPBE/6-311+(2d,p). However, a BP was detected for $^{20}C_{cape}$-∗-$^{18'}H_{cape}$ but not for $^{20}H_{cape}$-∗-$^{18'}H_{cape}$. The difference in the atomic size between C and H, such as the van der Waals radii, may be responsible for the predicted results, in this case. The $^{20}C_{cape}$-∗-$^{18'}H_{cape}$, $^{20}H_{cape}$-∗-$^{20'}H_{bay}$, $^{20}H_{cape}$-∗-$^{2'}C_{cape}$, and $^8H_{cape}$-∗-$^{3'}C_{cape}$ distances at **7:7**, optimized with LC-ωPBE/6-311+(2d,p), were much longer than the corresponding distances, optimized with M06-2X/6-311+(2d,p). BPs were detected for $^{20}H_{cape}$-∗-$^{18'}H_{cape}$, $^{20}H_{cape}$-∗-$^{20'}H_{bay}$, $^{20}H_{cape}$-∗-$^{2'}C_{cape}$, and $^{18}H_{cape}$-∗-$^{3'}C_{cape}$ when calculated with M06-2X/6-311+(2d,p), while they were detected for $^{20}C_{cape}$-∗-$^{18'}H_{cape}$, $^{20}H_{cape}$-∗-$^{20'}H_{bay}$, $^{20}H_{cape}$-∗-$^{2'}C_{cape}$, and $^8H_{cape}$-∗-$^{3'}C_{cape}$ when calculated with LC-ωPBE/6-311+(2d,p). The differences in the optimized distances appear to be the main factor for the appearance/disappearance of the BPs, similar to the case of **7**.

Table 3 contains the ν_1 values for **7** and **7:7**, calculated with M06-2X/6-311+(3d,p), M06-2X/6-311+(2d,p), and LC-ωPBE/6-311+(2d,p). Table 3 also contains some vibrations closely related to the interactions in question (corresponding to the perturbed structures) at **7:7**, where most candidates were found to be less than ν_n of ν_{20}. The ν_1 values for **7** were 48.4 cm^{-1}, 46.6 cm^{-1}, and 40.2 cm^{-1} when calculated with the three methods, respectively. The ν_1 motion of **7** appears to be very similar when calculated with the three methods. In the case of **7:7**, the frequencies of ν_1 calculated with M06-2X/6-311+G(3d,p) and M06-2X/6-311+G(2d,p) were 14.0 cm^{-1} and 13.1 cm^{-1}, respectively, while the value calculated with LC-ωPBE was 2.1 cm^{-1}. Very large differences are predicted for ν_1 at **7:7** when calculated at the M06-2X and LC-ωPBE levels. The ν_1 value with the motion should correspond to the strength of the interactions in the direction of the perturbed structures.

The (θ, θ_p) values of **7:7** are (67.9–73.0°, 69.4–75.2°) and (62.9–67.2°, 67.4–73.9°) with M06-2X/6-311+(2d,p) and LC-ωPBE/6-311+(2d,p), respectively. The differences seem large

relative to the case of **7**, with $(\theta, \theta_\mathrm{p})$ values of $(70.4°, 81.6°)$ and $(70.5°, 82.2°)$ when calculated with M06-2X/6-311+(2d,p) and LC-ωPBE/6-311+(2d,p), respectively, although **7** ($^1\mathrm{H_{bay}}$-*-$^6\mathrm{C_{bay}}$) was detected with M06-2X/6-311+(2d,p) and **7** ($^1\mathrm{H_{bay}}$-*-$^5\mathrm{C_{bay}}$) was detected with LC-ωPBE/6-311+(2d,p). The (optimized) structures of **7:7** would be affected more easily by surroundings containing the calculation methods than the case of **7**. The basis set and level dependence of the interactions in **7** and **7:7** can help us to better understand the interactions in helicenes.

The unit of C_{ii} [Å mdyn^{-1}] is the inverse of that of the force constant, which corresponds to the frequency. Therefore, the strengths of the interactions should be roughly inversely proportional to the C_{ii} values. As shown in Table 3, the C_{ii} values for the $\pi\cdots\pi$ interactions of **7** are 3.1–5.5 Å mdyn^{-1} for $\mathrm{H_{bay}}$-*-$\mathrm{C_{bay}}$ and $\mathrm{C_{bay}}$-*-$\mathrm{C_{bay}}$ with the three methods. The values for the $\pi\cdots\pi$ interactions of **7:7** are 10.0–27.9, 11.4–31.4, and 52.7–96.4 Å mdyn^{-1} for $\mathrm{H_{cape}}$-*-$\mathrm{H_{cape}}$ and $\mathrm{H_{cape}}$-*-$\mathrm{C_{cape}}$ when calculated with M06-2X/6-311+(3d,p), M06-2X/6-311+(2d,p), and LC-ωPBE/6-311+(2d,p), respectively. This consideration explains the above results.

5. Conclusions

It is challenging to clarify the natures of $\pi\cdots\pi$ interactions in helicenes since the interactions are factors that control the fine details of structures and are expected to give rise to specific functionalities for the species. The repulsive interactions between the benzene rings in helicenes must be very strong; therefore, the $\pi\cdots\pi$ interactions would be considered strong. The $\pi\cdots\pi$ interactions in the helicenes are described by the H-*-H, C-*-H, and C-*-C forms with BPs and BCPs. The $\pi\cdots\pi$ interactions in helicenes **1**–**12**, as well as in dimers **6:6** and **7:7**, were analyzed with QTAIM-DFA after clarifying the structural features and the energy profile. $H_\mathrm{b}(r_\mathrm{c})$ was plotted versus $H_\mathrm{b}(r_\mathrm{c}) - V_\mathrm{b}(r_\mathrm{c})/2$, and the data from the fully optimized structures and the perturbed structures around the fully optimized structures were used in QTAIM-DFA. Data from the fully optimized structures in the plots correspond to the static nature of the interactions, which are analyzed using polar coordinate (R, θ) representation. Data from both the perturbed and fully optimized structures are expressed by $(\theta_\mathrm{p}, \kappa_\mathrm{p})$, where θ_p corresponds to the tangent line and κ_p is the curvature of the plot. The concept of the dynamic nature of the interactions was proposed based on $(\theta_\mathrm{p}, \kappa_\mathrm{p})$.

The interactions were analyzed by dividing the C atoms of **3**–**12** into $\mathrm{C_{bay}}$ and $\mathrm{C_{cape}}$ and the H atoms into $\mathrm{H_{bay}}$ and $\mathrm{H_{cape}}$. While both $\mathrm{C_{bay}}$ and $\mathrm{C_{cape}}$ atoms of **3**–**12** take part in the interactions, only $\mathrm{H_{bay}}$ atoms participate as BPs. The θ and θ_p values for H-*-H, C-*-H, and C-*-C of **3**–**12** are all less than 90°, except for **10** ($^2\mathrm{C_{bay}}$-*-$^7\mathrm{C_{bay}}$), where $(\theta, \theta_\mathrm{p}) = (70.5°, 94.2°)$. Therefore, the H-*-H, C-*-H, and C-*-C interactions of **3**–**12** are all predicted to have a *p*-CS/vdW nature, except for **10** ($^2\mathrm{C_{bay}}$-*-$^7\mathrm{C_{bay}}$), which is predicted to have a *p*-CS/*t*-HB$_\mathrm{nc}$ nature. While the $(\theta, \theta_\mathrm{p})$ values of $\mathrm{C_{bay}}$-*-$\mathrm{C_{bay}}$ in **7**–**12** are (71.5–72.9°, 79.5–87.8°), the values are (70.0–70.7°, 66.3–69.7°) for $\mathrm{C_{cape}}$-*-$\mathrm{C_{cape}}$. The θ values for $\mathrm{C_{cape}}$-*-$\mathrm{C_{cape}}$ are slightly smaller than those of $\mathrm{C_{bay}}$-*-$\mathrm{C_{bay}}$ (by 0.5–2.2°), but the θ_p values for $\mathrm{C_{cape}}$-*-$\mathrm{C_{cape}}$ are much smaller than those of $\mathrm{C_{bay}}$-*-$\mathrm{C_{bay}}$ (by 13.2–24.5°). In this case, $\theta < \theta_\mathrm{p}$ for $\mathrm{C_{bay}}$-*-$\mathrm{C_{bay}}$, whereas $\theta > \theta_\mathrm{p}$ for $\mathrm{C_{cape}}$-*-$\mathrm{C_{cape}}$. Interactions with $\theta < \theta_\mathrm{p}$ are usually observed, whereas interactions with $\theta > \theta_\mathrm{p}$ are rare.

The H-*-H, C-*-H, and C-*-C interactions of dimers **6:6** and **7:7** were similarly analyzed. The interactions were predicted to have a *p*-CS/vdW nature, although **6:6** ($^1\mathrm{H_{bay}}$-*-$^{17'}\mathrm{H_{cape}}$) has a nature close to *p*-CS/*t*-HB$_\mathrm{nc}$, since $(\theta, \theta_\mathrm{p}) = (72.6°, 88.1°)$. The interactions at **3**–**12** and **6:6** and **7:7** were predicted to be much weaker than expected. The very low energy of ν_1 of **7:7** supports the very weak nature predicted for interactions and the easy dependence of the levels on the nature of the interactions. The strength of the interactions can also be estimated by the C_{ii}^{-1} values. Detecting the interactions and predicting the nature of helicenes will provide a solid basis for investigating and applying the interactions in helicenes.

Supplementary Materials: The following are available online at https://www.mdpi.com/article/10.3390/nano12030321/s1. Table S1: The observed and calculated C···C length (r_{obsd} and r_{calcd}, respectively), which are located in the bay area for **3**–**5** and the bay and cape area between adjacent aromatic rings for **6**–**12**, together with the differences, Δr_{calcd} (=$r_{calcd:XY} - r_{obsd:XY}$) in each C···C for **3**–**12**, elucidated with various methods. Table S2: The total energy E_{ES} and zero-point energy E_{ZP} values for n; n_p, where $n = 1$ to 12, along with the ΔE_{ES} and $\Delta E_{ZP}(n; n_p)$ values, evaluated with M06-2X/6-311+G(3d,p). Table S3: The HOMA indices for [n]acenes, [n]phenacenes, and [n]helicenes, evaluated with M06-2X/6-311+G(3d,p). Table S4: The observed and calculated X-∗-Y lengths ($R_{obsd:XY}$ and $R_{calcd:XY}$, respectively; X, Y = C and H) and the length of the bond paths ($r_{BP:XY}$) and the corresponding straight-line distances ($R_{SL:XY}$), together with the differences, $\Delta R_{calcd:XY}$ (=$R_{calcd:XY} - R_{obsd:XY}$) in each X-∗-Y for **3**–**12**, **6:6** and **7:7**, evaluated with M06-2X/6-311+G(3d,p), where $R_{SL:XY} = R_{calcd:XY}$, together with **8:8** and **10:10**, calculated with M06-2X/6-311+G(2d,p). Table S5: QTAIM functions and QTAIM-DFA parameters for the fused benzene-type helicenes of monomers (**3**–**12** (C_2)), together with the nature of each noncovalent interaction, elucidated with M06-2X/6-311+G(2d,p). Table S6: QTAIM functions and QTAIM-DFA parameters for the fused benzene-type helicenes of monomers (**3**–**12** (C_2)), along with the nature of each noncovalent interaction, elucidated with LC-ωPBE/6-311+G(2d,p). Table S7: The E_{ES} (au), ΔE_{ES} (kJ mol^{-1}), and ΔE_{ZP} (kJ mol^{-1}) values for **6:6**–**8:8** and **10:10**, evaluated with various methods. Table S8: QTAIM functions and QTAIM-DFA parameters for the concave-type dimer of helicenes (**8:8**–**10:10** (C_i)), together with the nature of each noncovalent interaction, elucidated with M06-2X/6-311+G(2d,p). Figure S1: Plots of $\Delta E_{ZP}(n)$ versus $\Delta E_{ES}(n)$, calculated with M06-2X/6-311+G(3d,p). Figure S2: Plots of HOMA indices for [n]acenes ($n = 4$–12) at closed-shell singlet state, [n]acenes ($n = 7$–12) at open-shell singlet state, and [n]phenacenes ($n = 4$–12) versus those for [n]helicenes ($n = 4$–12), calculated with MP2/6-311+G(3d,p). Figure S3: Molecular graphs for **3**–**6**, **8**, and **10** calculated with M06-2X/6-311+G(3d,p). Figure S4: Plots of r_{BP} versus R_{SL} for H$_{bay}$-∗-H$_{bay}$, C$_{bay}$-∗-H$_{bay}$, C$_{bay}$-∗-C$_{bay}$, and C$_{cape}$-∗-C$_{cape}$ in **3**–**12**, calculated with M06-2X/6-311+G(3d,p). Figure S5: Plots of $H_b(r_c)$ versus $H_b(r_c) - V_b(r_c)/2$ for H-∗-H, C-∗-H, and C-∗-C for **7**, **9**, and **11**. Figure S6: Molecular graphs for **8:8** (C_i) and **10:10** (C_i) calculated with M06-2X/6-311+G(2d,p). Figure S7: Plots of $H_b(r_c)$ versus $H_b(r_c) - V_b(r_c)/2$ for H-∗-H, C-∗-H, and C-∗-C for **8:8** and **10:10**. Figure S8: The internal vibration motions of ν_n for **7:7** (C_i) from the top view. Figure S9: The internal vibration motions of ν_n for **7:7** (C_i).

Author Contributions: S.H. formulated the project. T.N. and S.H. optimized all compounds. T.N. calculated the $\rho_b(r_c)$, $H_b(r_c) - V_b(r_c)/2$ (=$(\hbar^2/8m)\nabla^2\rho_b(r_c)$), and $H_b(r_c)$ values, evaluated the QTAIM-DFA parameters, and analyzed the data. S.H. and T.N. organized the data for writing, and T.N. wrote the paper. All authors have read and agreed to the published version of the manuscript.

Data Availability Statement: Data are contained within the article or the Supplementary Materials.

Conflicts of Interest: The authors declare no conflict of interest.

References

1. Shen, Y.; Chen, C.F. Helicenes: Synthesis and Applications. *Chem. Rev.* **2012**, *112*, 1463–1535. [CrossRef] [PubMed]
2. Chen, C.F.; Shen, Y. *Helicene Chemistry: From Synthesis to Applications*; Springer: Berlin, Germany, 2017. [CrossRef]
3. Dhbaibi, K.; Favereau, L.; Crassous, J. Enantioenriched Helicenes and Helicenoids Containing Main-Group Elements (B, Si, N, P). *Chem. Rev.* **2019**, *119*, 8846–8953. [CrossRef] [PubMed]
4. Tani, F.; Narita, M.; Murafuji, T. Helicene Radicals: Molecules Bearing a Combination of Helical Chirality and Unpaired Electron Spin. *ChemPlusChem* **2020**, *85*, 2093–2104. [CrossRef] [PubMed]
5. Jakubec, M.; Storch, J. Recent Advances in Functionalizations of Helicene Backbone. *J. Org. Chem.* **2020**, *85*, 13415–13428. [CrossRef]
6. Ren, M.; Wang, J.; Xie, X.; Zhang, J.; Wang, P. Double-Helicene-Based Hole-Transporter for Perovskite Solar Cells with 22% Efficiency and Operation Durability. *ACS Energy Lett.* **2019**, *4*, 2683–2688. [CrossRef]
7. Xu, N.; Li, Y.; Ricciarelli, D.; Wang, J.; Mosconi, E.; Yuan, Y.; de Angelis, F.; Zakeeruddin, S.M.; Grätzel, M.; Wang, P. An Oxa[5]Helicene-Based Racemic Semiconducting Glassy Film for Photothermally Stable Perovskite Solar Cells. *iScience* **2019**, *15*, 234–242. [CrossRef]

8. Wang, J.; Shi, H.; Xu, N.; Zhang, J.; Yuan, Y.; Lei, M.; Wang, L.; Wang, P. Aza[5]Helicene Rivals N-Annulated Perylene as π-Linker of D-π-D Typed Hole-Transporters for Perovskite Solar Cells. *Adv. Funct. Mater.* **2020**, *30*, 2002114. [CrossRef]

9. Wei, Y.; Zheng, A.; Xie, X.; Zhang, J.; He, L.; Wang, P. A Pyrrole-Bridged Bis(Oxa[5]Helicene)-Based Molecular Semiconductor for Efficient and Durable Perovskite Solar Cells: Microscopic Insights. *ACS Mater. Lett.* **2021**, *3*, 947–955. [CrossRef]

10. Wang, J.; Wang, Y.; Xie, X.; Ren, Y.; Zhang, B.; He, L.; Zhang, J.; Wang, L.D.; Wang, P. A Helicene-Based Molecular Semiconductor Enables 85 °C Stable Perovskite Solar Cells. *ACS Energy Lett.* **2021**, *6*, 1764–1772. [CrossRef]

11. Tsujihara, T.; Inada-Nozaki, N.; Takehara, T.; Zhou, D.Y.; Suzuki, T.; Kawano, T. Nickel-Catalyzed Construction of Chiral 1-[6]Helicenols and Application in the Synthesis of [6]Helicene-Based Phosphinite Ligands. *Eur. J. Org. Chem.* **2016**, *2016*, 4948–4952. [CrossRef]

12. Yamamoto, K.; Shimizu, T.; Igawa, K.; Tomooka, K.; Hirai, G.; Suemune, H.; Usui, K. Rational Design and Synthesis of [5]Helicene-Derived Phosphine Ligands and Their Application in Pd-Catalyzed Asymmetric Reactions. *Sci. Rep.* **2016**, *6*, 36211. [CrossRef]

13. Demmer, C.S.; Voituriez, A.; Marinetti, A. Catalytic Uses of Helicenes Displaying Phosphorus Functions. *Comptes Rendus Chim.* **2017**, *20*, 860–879. [CrossRef]

14. Cauteruccio, S.; Licandro, E.; Panigati, M.; D'Alfonso, G.; Maiorana, S. Modifying the Properties of Organic Molecules by Conjugation with Metal Complexes: The Case of Peptide Nucleic Acids and of the Intrinsically Chiral Thiahelicenes. *Coord. Chem. Rev.* **2019**, *386*, 119–137. [CrossRef]

15. Beránek, T.; Žádný, J.; Strašák, T.; Karban, J.; Císařová, I.; Sýkora, J.; Storch, J. Synthesis of a Helical Phosphine and a Catalytic Study of Its Palladium Complex. *ACS Omega* **2020**, *5*, 882–892. [CrossRef]

16. Medena, C.; Aubert, C.; Derat, E.; Fensterbank, L.; Gontard, G.; Khaled, O.; Ollivier, C.; Vanthuyne, N.; Petit, M.; Barbazanges, M. Helical Bisphosphinites in Asymmetric Tsuji-Trost Allylation: A Remarkable P:Pd Ratio Effect. *ChemCatChem* **2021**, *13*, 4543–4548. [CrossRef]

17. Kel, O.; Fürstenberg, A.; Mehanna, N.; Nicolas, C.; Laleu, B.; Hammarson, M.; Albinsson, B.; Lacour, J.; Vauthey, E. Chiral Selectivity in the Binding of [4]Helicene Derivatives to Double-Stranded DNA. *Chem. Eur. J.* **2013**, *19*, 7173–7180. [CrossRef]

18. Kawara, K.; Tsuji, G.; Taniguchi, Y.; Sasaki, S. Synchronized Chiral Induction between [5]Helicene–Spermine Ligand and B-Z DNA Transition. *Chem. Eur. J.* **2017**, *23*, 1763–1769. [CrossRef]

19. Kalachyova, Y.; Guselnikova, O.; Elashnikov, R.; Panov, I.; Žádný, J.; Církva, V.; Storch, J.; Sykora, J.; Zaruba, K.; Švorčík, V.; et al. Helicene-SPP-Based Chiral Plasmonic Hybrid Structure: Toward Direct Enantiomers SERS Discrimination. *ACS Appl. Mater. Interfaces* **2019**, *11*, 1555–1562. [CrossRef]

20. Schulte, T.R.; Holstein, J.J.; Clever, G.H. Chiral Self-Discrimination and Guest Recognition in Helicene-Based Coordination Cages. *Angew. Chem.* **2019**, *131*, 5618–5622. [CrossRef]

21. Petdum, A.; Faichu, N.; Sirirak, J.; Khammultri, P.; Promarak, V.; Panchan, W.; Sooksimuang, T.; Charoenpanich, A.; Wanichacheva, N. [5]Helicene-Rhodamine 6 G Hybrid-Based Sensor for Ultrasensitive Hg^{2+} Detection and Its Biological Applications. *J. Photochem. Photobiol. A* **2020**, *394*, 112473. [CrossRef]

22. Gu, X.H.; Lei, Y.; Wang, S.; Cao, F.; Zhang, Q.; Chen, S.; Wang, K.P.; Hu, Z.Q. Tetrahydro[5]Helicene Fused Nitrobenzoxadiazole as a Fluorescence Probe for Hydrogen Sulfide, Cysteine/Homocysteine and Glutathione. *Spectrochim. Acta A Mol. Biomol. Spectrosc.* **2020**, *229*, 118003. [CrossRef]

23. Li, J.; Martin, K.; Avarvari, N.; Wäckerlin, C.; Ernst, K.H. Spontaneous Separation of On-Surface Synthesized Tris-Helicenes into Two-Dimensional Homochiral Domains. *Chem. Commun.* **2018**, *54*, 7948–7951. [CrossRef]

24. Shiotari, A.; Tanaka, K.; Nakae, T.; Mori, S.; Okujima, T.; Uno, H.; Sakaguchi, H.; Sugimoto, Y. Chiral Discrimination and Manipulation of Individual Heptahelicene Molecules on Cu(001) by Noncontact Atomic Force Microscopy. *J. Phys. Chem. C* **2018**, *122*, 4997–5003. [CrossRef]

25. Zhang, H.; Liu, H.; Shen, C.; Gan, F.; Su, X.; Qiu, H.; Yang, B.; Yu, P. Chiral Recognition of Hexahelicene on a Surface via the Forming of Asymmetric Heterochiral Trimers. *Int. J. Mol. Sci.* **2019**, *20*, 2018. [CrossRef]

26. Irziqat, B.; Berger, J.; Mendieta-Moreno, J.I.; Sundar, M.S.; Bedekar, A.V.; Ernst, K.H. Transition from Homochiral Clusters to Racemate Monolayers during 2D Crystallization of Trioxa[11]Helicene on Ag(100). *ChemPhysChem* **2021**, *22*, 293–297. [CrossRef]

27. Matsuiwa, K.; Hayashi, S.; Nakanishi, W. Dynamic and Static Behavior of Intramolecular π-π Interactions in [2.2]- and [3.3]Cyclophanes, Elucidated by QTAIM Dual Functional Analysis with QC Calculations. *ChemistrySelect* **2017**, *2*, 1774–1782. [CrossRef]

28. Matsuiwa, K.; Hayashi, S.; Nakanishi, W. Intramolecular π-π Interactions in Diethanodihydronaphthalene and Derivatives: Dynamic and Static Behavior of the Interactions Elucidated by QTAIM Dual Functional Analysis. *ChemistrySelect* **2016**, *1*, 2344–2353. [CrossRef]

29. Matsuiwa, K.; Sugibayashi, Y.; Tsubomoto, Y.; Hayashi, S.; Nakanishi, W. Behavior of Intramolecular π-π Interactions with Doubly Degenerated Bond Paths between Carbon Atoms in Opposite Benzene Rings of Diethenodihydronaphthalenes by QTAIM Approach. *ChemistrySelect* **2017**, *2*, 90–100. [CrossRef]

30. Nakanishi, W.; Hayashi, S.; Narahara, K. Atoms-in-Molecules Dual Parameter Analysis of Weak to Strong Interactions: Behaviors of Electronic Energy Densities versus Laplacian of Electron Densities at Bond Critical Points. *J. Phys. Chem. A* **2008**, *112*, 13593–13599. [CrossRef]

31. Nakanishi, W.; Hayashi, S.; Narahara, K. Polar Coordinate Representation of $H_b(r_c)$ versus $(\hbar^2/8m)\nabla^2\rho_b(r_c)$ at BCP in AIM Analysis: Classification and Evaluation of Weak to Strong Interactions. *J. Phys. Chem. A* **2009**, *113*, 10050–10057. [CrossRef]

32. Nakanishi, W.; Hayashi, S. Atoms-in-Molecules Dual Functional Analysis of Weak to Strong Interactions. *Curr. Org. Chem.* **2010**, *14*, 181–197. [CrossRef]

33. Nakanishi, W.; Hayashi, S. Dynamic Behaviors of Interactions: Application of Normal Coordinates of Internal Vibrations to AIM Dual Functional Analysis. *J. Phys. Chem. A* **2010**, *114*, 7423–7430. [CrossRef] [PubMed]

34. Nakanishi, W.; Hayashi, S.; Matsuiwa, K.; Kitamoto, M. Applications of Normal Coordinates of Internal Vibrations to Generate Perturbed Structures: Dynamic Behavior of Weak to Strong Interactions Elucidated by Atoms-in-Molecules Dual Functional Analysis. *Bull. Chem. Soc. Jpn.* **2012**, *85*, 1293–1305. [CrossRef]

35. Nakanishi, W.; Hayashi, S. Role of dG/dw and dV/dw in AIM Analysis: An Approach to the Nature of Weak to Strong Interactions. *J. Phys. Chem. A* **2013**, *117*, 1795–1803. [CrossRef]

36. Bader, R.F.W. *Atoms in Molecules. A Quantum Theory*; Oxford University Press: Oxford, UK, 1990.

37. Matta, C.F.; Boyd, R.J. An introduction to the quantum theory of atoms in molecules. In *The Quantum Theory of Atoms in Molecules: From Solid State to DNA and Drug Design*; Wiley: Weinheim, Germany, 2007. [CrossRef]

38. Nakanishi, W.; Hayashi, S. Perturbed Structures Generated Using Coordinates Derived from Compliance Constants in Internal Vibrations for QTAIM Dual Functional Analysis: Intrinsic Dynamic Nature of Interactions. *Int. J. Quantum Chem.* **2018**, *118*, e25590. [CrossRef]

39. Grunenberg, J.; Brandhorst, K. Compliance 3.0.2 program. Available online: http://www.oc.tu--bs.de/Grunenberg/compliance.html (accessed on 14 December 2021).

40. Brandhorst, K.; Grunenberg, J. Efficient Computation of Compliance Matrices in Redundant Internal Coordinates from Cartesian Hessians for Nonstationary Points. *J. Chem. Phys.* **2010**, *132*, 184101. [CrossRef]

41. Brandhorst, K.; Grunenberg, J. How Strong Is It? The Interpretation of Force and Compliance Constants as Bond Strength Descriptors. *Chem. Soc. Rev.* **2008**, *37*, 1558–1567. [CrossRef]

42. Grunenberg, J. Ill-Defined Concepts in Chemistry: Rigid Force Constants vs. Compliance Constants as Bond Strength Descriptors for the Triple Bond in Diboryne. *Chem. Sci.* **2015**, *6*, 4086–4088. [CrossRef]

43. Grunenberg, J. Direct Assessment of Interresidue Forces in Watson-Crick Base Pairs Using Theoretical Compliance Constants. *J. Am. Chem. Soc.* **2004**, *126*, 16310–16311. [CrossRef]

44. Grunenberg, J.; Barone, G. Are Compliance Constants Ill-Defined Descriptors for Weak Interactions? *RSC Adv.* **2013**, *3*, 4757–4762. [CrossRef]

45. Taylor, W.J.; Pitzer, K.S. Vibrational Frequencies of Semirigid Molecules: A General Method and Values for Ethylbenzene. *J. Res. Natl. Bur. Stand.* **1947**, *38*, 1–17. [CrossRef]

46. Konkoli, Z.; Cremer, D. A New Way of Analyzing Vibrational Spectra. I. Derivation of Adiabatic Internal Modes. *Int. J. Quantum Chem.* **1998**, *67*, 1–9. [CrossRef]

47. Grunenberg, J.; Goldberg, N. How Strong Is the Gallium≡Gallium Triple Bond? Theoretical Compliance Matrices as a Probe for Intrinsic Bond Strengths. *J. Am. Chem. Soc.* **2000**, *122*, 6045–6047. [CrossRef]

48. Grunenberg, J.; Streubel, R.; Frantzius, G.V.; Marten, W. The Strongest Bond in the Universe? Accurate Calculation of Compliance Matrices for the Ions N_2H^+, HCO^+, and HOC^+. *J. Chem. Phys.* **2003**, *119*, 165–169. [CrossRef]

49. Xie, Y.; Schaefer, H.F. The Characterization of Metal–Metal Bonds in Unsaturated Binuclear Homoleptic Transition Metal Carbonyls. The Compliance Matrix. *Z. Phys. Chem.* **2003**, *217*, 189–203. [CrossRef]

50. Frisch, M.J.; Trucks, G.W.; Schlegel, H.B.; Scuseria, G.E.; Robb, M.A.; Cheeseman, J.R.; Scalmani, G.; Barone, V.; Mennucci, B.; Petersson, G.A.; et al. *Gaussian 09 (Revision D.01)*; Gaussian, Inc.: Wallingford, CT, USA, 2009.

51. Zhao, Y.; Truhlar, D.G. The M06 Suite of Density Functionals for Main Group Thermochemistry, Thermochemical Kinetics, Noncovalent Interactions, Excited States, and Transition Elements: Two New Functionals and Systematic Testing of Four M06-Class Functionals and 12 Other Functionals. *Theor. Chem. Acc.* **2008**, *120*, 215–241. [CrossRef]

52. Vydrov, O.A.; Scuseria, G.E. Assessment of a Long–Range Corrected Hybrid Functional. *J. Chem. Phys.* **2006**, *125*, 234109. [CrossRef]

53. Hayashi, S.; Nishide, T.; Ueda, K.; Hayami, K.; Nakanishi, W. Effects from Basis Sets and Levels of Calculations on the Nature of Interactions Predicted by QTAIM-Dual Functional Analysis with QTAIM Functions. *ChemistrySelect* **2019**, *4*, 6198–6208. [CrossRef]

54. Ivanov, M.D.; Kirina, Y.V.; Novikov, A.S.; Starova, G.L.; Kukushkin, V.Y. Efficient π–stacking with benzene provides 2D assembly of trans–[PtCl$_2$(p–CF$_3$C$_6$H$_4$CN)$_2$]. *J. Mol. Struct.* **2016**, *1104*, 19–23. [CrossRef]

55. Mukhacheva, A.A.; Komarov, V.Y.; Kokovkin, V.V.; Novikov, A.S.; Abramov, P.A.; Sokolov, M.N. Unusual p-p interactions directed by the [{(C$_6$H$_6$)Ru}$_2$W$_8$O$_{30}$(OH)$_2$]$^{6-}$ hybrid anion. *CrystEngComm* **2021**, *23*, 4125–4135. [CrossRef]

56. Biegler–König, F.; Schönbohm, J. The AIM2000 Program (Version 2.0). Available online: http://www.aim2000.de (accessed on 14 December 2021).

57. Biegler–König, F. Calculation of atomic integration data. *J. Comput. Chem.* **2000**, *21*, 1040–1048. [CrossRef]

58. Keith, T.A. AIMAll (Version 17.11.14), TK Gristmill Software, Overland Park, KS, USA. 2017. Available online: http://aim.tkgristmill.com (accessed on 14 December 2021).

59. Kay, M.I.; Okaya, Y.; Cox, D.E. A Refinement of the Structure of the Room–Temperature Phase of Phenanthrene, C$_{14}$H$_{10}$, from X-ray and Neutron Diffraction Data. *Acta Crystallogr. Sect. B Struct. Crystallogr. Cryst. Chem.* **1971**, *27*, 26–33. [CrossRef]

60. Lakshman, M.K.; Kole, P.L.; Chaturvedi, S.; Saugier, J.H.; Yeh, H.J.C.; Glusker, J.P.; Carrell, H.L.; Katz, A.K.; Afshar, C.E.; Dashwood, W.M.; et al. Methyl Group-Induced Helicity in 1,4-Dimethylbenzo[c]Phenanthrene and Its Metabolites: Synthesis, Physical, and Biological Properties. *J. Am. Chem. Soc.* **2000**, *122*, 12629–12636. [CrossRef]

61. Bédard, A.C.; Vlassova, A.; Hernandez-Perez, A.C.; Bessette, A.; Hanan, G.S.; Heuft, M.A.; Collins, S.K. Synthesis, Crystal Structure and Photophysical Properties of Pyrene-Helicene Hybrids. *Chem. Eur. J.* **2013**, *19*, 16295–16302. [CrossRef]

62. Yoshida, Y.; Nakamura, Y.; Kishida, H.; Hayama, H.; Nakano, Y.; Yamochi, H.; Saito, G. Racemic Charge–Transfer Complexes of a Helical Polycyclic Aromatic Hydrocarbon Molecule. *CrystEngComm* **2017**, *19*, 3626–3632. [CrossRef]

63. Fujino, S.; Yamaji, M.; Okamoto, H.; Mutai, T.; Yoshikawa, I.; Houjou, H.; Tani, F. Systematic Investigations on Fused π-System Compounds of Seven Benzene Rings Prepared by Photocyclization of Diphenanthrylethenes. *Photochem. Photobiol. Sci.* **2017**, *16*, 925–934. [CrossRef]

64. Mori, K.; Murase, T.; Fujita, M. One-Step Synthesis of [16]Helicene. *Angew. Chem.* **2015**, *127*, 6951–6955. [CrossRef]

65. Bas, G.L.; Navaza, A.; Mauguen, Y.; Rango, C.D. 10-Helicene, C42H24. *Cryst. Struct. Commun.* **1976**, *5*, 357–361.

66. Bas, G.L.; Navaza, A.; Knossow, M.; Rango, C.D. 11-Helicene, C46H26. *Cryst. Struct. Commun.* **1976**, *5*, 713–718.

67. Rulíšek, L.; Exner, O.; Cwiklik, L.; Jungwirth, P.; Starý, I.; Pospíšil, L.; Havias, Z. On the Convergence of the Physicochemical Properties of [*n*]Helicenes. *J. Phys. Chem. C* **2007**, *111*, 14948–14955. [CrossRef]

68. Krygowski, T.M. Crystallographic Studies of Inter– and Intramolecular Interactions Reflected in Aromatic Character of π–Electron Systems. *J. Chem. Inf. Comput. Sci.* **1993**, *33*, 70–78. [CrossRef]

69. Bader, R.F.W. Bond Paths Are Not Chemical Bonds. *J. Phys. Chem. A* **2009**, *113*, 10391–10396. [CrossRef]

70. Grimme, S.; Mück-Lichtenfeld, C.; Erker, G.; Kehr, G.; Wang, H.; Beckers, H.; Willner, H. When Do Interacting Atoms Form a Chemical Bond? Spectroscopic Measurements and Theoretical Analyses of Dideuteriophenanthrene. *Angew. Chem. Int.* **2009**, *48*, 2592–2595. [CrossRef]

71. Cukrowski, I. A Unified Molecular–Wide and Electron Density Based Concept of Chemical Bonding. *Wiley Interdiscip. Rev. Comput. Mol. Sci.* **2021**, e1579. [CrossRef]

72. Pendás, A.M.; Francisco, E.; Blanco, M.A.; Gatti, C. Bond Paths as Privileged Exchange Channels. *Chem. Eur. J.* **2007**, *13*, 9362–9371. [CrossRef]

73. Tognetti, V.; Joubert, L. On the Physical Role of Exchange in the Formation of an Intramolecular Bond Path between Two Electronegative Atoms. *J. Chem. Phys.* **2013**, *138*, 024102. [CrossRef]

74. Cukrowski, I.; de Lange, J.H.; Adeyinka, A.S.; Mangondo, P. Evaluating Common QTAIM and NCI Interpretations of the Electron Density Concentration through IQA Interaction Energies and 1D Cross–Sections of the Electron and Deformation Density Distributions. *Comput. Theor. Chem.* **2015**, *1053*, 60–76. [CrossRef]